UvA-DARE (Digital Academic Repository)

Investigating the spectroscopic, magnetic and circumstellar variability of the O9 subgiant star HD 57682

Grunhut, J.H.; Wade, G.A.; Sundqvist, J.O.; ud-Doula, A.; Neiner, C.; Ignace, R.; Marcolino, W.L.F.; Rivinius, T.; Fullerton, A.; Kaper, L.; Mauclaire, B.; Buil, C.; Garrel, T.; Ribeiro, J.; Ubaud, S.

Link to publication

Investigating the spectroscopic, magnetic and circumstellar variability of the O9 subgiant star HD 57682[★]

J. H. Grunhut,[1,2]† G. A. Wade,[2] J. O. Sundqvist,[3] A. ud-Doula,[4] C. Neiner,[5] R. Ignace,[6] W. L. F. Marcolino,[7] Th. Rivinius,[8] A. Fullerton,[9] L. Kaper,[10] B. Mauclaire,[11] C. Buil,[12] T. Garrel,[13] J. Ribeiro,[14] S. Ubaud[15] and the MiMeS Collaboration

[1]*Department of Physics, Engineering Physics and Astronomy, Queens University, Kingston, Ontario K7L 3N6, Canada*
[2]*Department of Physics, Royal Military College of Canada, PO Box 17000, Station Forces, Kingston, Ontario K7K 7B4, Canada*
[3]*University of Delaware, Bartol Research Institute, Newark, DE 19716, USA*
[4]*Penn State Worthington Scranton, 120 Ridge View Drive, Dunmore, PA 18512, USA*
[5]*LESIA, Observatoire de Paris, CNRS UMR 8109, UPMC, Université Paris Diderot, 5 place Jules Janssen, 92190 Meudon, France*
[6]*Department of Physics and Astronomy, East Tennessee State University, Johnson City, TN 37614, USA*
[7]*Universidade Federal do Rio de Janeiro, Observatório do Valongo Ladeira Pedro Antônio 43, CEP 20080-090 Rio de Janeiro, Brazil*
[8]*ESO – European Organisation for Astronomical Research in the Southern Hemisphere, Casilla 19001, Santiago 19, Chile*
[9]*Space Telescope Science Institute, 3700 San Martin Drive, Baltimore, MD 21218, USA*
[10]*Astronomical Institute 'Anton Pannekoek', University of Amsterdam, Science Park 904, 1098 XH Amsterdam, the Netherlands*
[11]*Observatoire du Val de l'Arc, route de Peynier, 13530 Trets, France*
[12]*Castanet Tolosan Observatory, 6 place Clémence Isaure, 31320 Castanet Tolosan, France*
[13]*Observatoire de Juvignac, 19 avenue du Hameau du Golf, 34990 Juvignac, France*
[14]*Obervatorio do Instituto Geografico do Exercito, R. Venezuela 29, 3 Esq., 1500-618 Lisboa, Portugal*
[15]*Observatoire des Quatres chemins, Calade, 06410 Biot, France*

ABSTRACT

The O9IV star HD 57682, discovered to be magnetic within the context of the Magnetism in Massive Stars (MiMeS) survey in 2009, is one of only eight convincingly detected magnetic O-type stars. Among this select group, it stands out due to its sharp-lined photospheric spectrum. Since its discovery, the MiMeS Collaboration has continued to obtain spectroscopic and magnetic observations in order to refine our knowledge of its magnetic field strength and geometry, rotational period and spectral properties and variability. In this paper we report new Echelle SpectroPolarimetric Device for the Observation of Stars (ESPaDOnS) spectropolarimetric observations of HD 57682, which are combined with previously published ESPaDOnS data and archival Hα spectroscopy. This data set is used to determine the rotational period (63.5708 ± 0.0057 d), refine the longitudinal magnetic field variation and magnetic geometry (dipole surface field strength of 880 ± 50 G and magnetic obliquity of 79° ± 4° as measured from the magnetic longitudinal field variations, assuming an inclination of 60°) and examine the phase variation of various lines. In particular, we demonstrate that the Hα equivalent width undergoes a double-wave variation during a single rotation of the star, consistent with the derived magnetic geometry. We group the variable lines into two classes: those that, like Hα, exhibit non-sinusoidal variability, often with multiple maxima during the rotation cycle, and those that vary essentially sinusoidally. Based on our modelling of the Hα emission, we show that the variability is consistent with emission being generated from an optically thick, flattened distribution of magnetically confined plasma that is roughly distributed about the magnetic equator. Finally, we discuss our findings in the magnetospheric framework proposed in our earlier study.

1 INTRODUCTION

HD 57682 is an O9 subgiant, and one of only eight O-type stars convincingly detected to host magnetic fields: the zero-age main-sequence (ZAMS) O7V star θ^1 Ori C = HD 37022 (Donati et al. 2002; Wade et al. 2006), the more evolved Of?p stars HD 108 (Martins et al. 2010), HD 148937 (Hubrig et al. 2008; Wade et al. 2012a), HD 191612 (Donati et al. 2006; Wade et al. 2011), NGC 1624-2 (Wade et al. 2012b) and CPD −28 2561 (Hubrig et al. 2011b; Wade et al. 2012c), the recently detected Carina nebula star Tr16-22 (Nazé et al. 2012) and HD 57682 (Grunhut et al. 2009). In addition, a small number of other O-type stars have been tentatively reported to be magnetic in modern literature (e.g. Bouret et al. 2008; Hubrig et al. 2008; Hubrig, Oskinova & Schöller 2011a; Hubrig et al. 2011b). These stars have either been found through independent observation and/or analysis to be non-magnetic (e.g. Fullerton et al. 2011; Bagnulo et al. 2012), or have yet to be independently re-observed or re-analysed. These small numbers are both a reflection of the rarity of O-type stars with detectable magnetic fields, and the challenge of detecting such fields when present.

Based on seven spectropolarimetric observations of HD 57682, Grunhut et al. (2009) characterized its physical and wind properties, deriving, in particular, a mass of 17^{+19}_{-9} M$_\odot$, a radius of $7.0^{+2.4}_{-1.8}$ R$_\odot$, a mass-loss rate log $\dot{M} = -8.85$ M$_\odot$ yr^{-1} and wind terminal velocity $v_\infty = 1200^{+500}_{-200}$ km s^{-1}. Their spectroscopic and magnetic data indicated that the star was variable, likely periodically on a time-scale of a few weeks. Using the Bayesian statistical method of Petit & Wade (2012), Grunhut et al. (2009) estimated the surface dipole strength to be 1680^{+135}_{-355} G. This magnetic field strength, combined with the inferred physical and wind parameters, indicated a wind magnetic confinement parameter of 1.4×10^4 (ud-Doula & Owocki 2002), leading the authors to suggest that the observed line profile variations were a consequence of dense wind plasma confined in closed magnetic loops above the stellar surface.

The present study seeks to refine and elaborate the preliminary results reported by Grunhut et al. (2009). In Section 2 we discuss the new and archival observations used in our analysis, including extraction of least-squares deconvolved (LSD) mean profiles and measurement of the longitudinal magnetic field. In Section 3 we perform a period analysis of the Hα and longitudinal field data and demonstrate that a single period of ∼63 d is required to reproduce the periodic variations of the measurements, which span over 15 yr. In Section 4 we discuss the implications of the inferred rotation period for the projected rotational velocity of the star, and, in particular, the estimate of 15 km s^{-1} proposed by Grunhut et al. (2009). In Section 5 we constrain the magnetic field properties using the longitudinal field measurements and direct fits to the observed LSD Stokes V profiles. In Section 6 we present an extensive overview of the variability of line profiles of H, He and metals. In Section 7 we revisit the magnetospheric framework proposed by Grunhut et al. (2009), and in Section 8 we discuss our results and present our conclusions.

2 OBSERVATIONS

2.1 Polarimetric data and measurements

A total of 38 polarimetric observations were collected with the high-resolution ($R \sim 68\,000$) Echelle SpectroPolarimetric Device for the

Observation of Stars (ESPaDOnS) spectropolarimeter mounted on the Canada–France–Hawaii Telescope (CFHT). The observations were obtained in the context of the Magnetism in Massive Stars (MiMeS) CFHT Large Programme on 20 different nights over a period of 2 yr from 2008 December to 2010 December. Each observation consists of a sequence of four subexposures that were processed using the UPENA pipeline running LIBRE-ESPRIT, as described by Donati et al. (1997). The final reduced products consist of an unpolarized Stokes I and circularly polarized Stokes V spectrum. The individual subexposures are also combined in such a way that the polarization should cancel out, resulting in a diagnostic null spectrum that is used to test for spurious signals in the data. During most nights two polarimetric sequences were obtained and the unnormalized spectra were combined to produce 20 distinct observations. Seven of our 20 observations were previously discussed by Grunhut et al. (2009) and we present 13 new observations here, the details of which are listed in Table 1. In Fig. 1 we show spectra for selected spectral regions at a few different rotational phases to highlight the variability observed in almost all spectral lines (see Section 3 for further details).

From each observation we extracted LSD profiles using the technique as described by Donati et al. (1997). The measurements reported here differ in details from those reported by Grunhut et al. (2009) as we have adopted an updated line mask with significantly more lines, but the measurements are fully consistent within their respective uncertainties. Our new mask has an average Landé factor and average wavelength of 1.180 and 4682 Å versus 1.135 and 4649 Å from the original mask. The new mask was derived from the Vienna Atomic Line Database (VALD; Piskunov et al. 1995) for a $T_{\mathrm{eff}} = 35\,000$ K, log $(g) = 4.0$ model atmosphere. Only lines with intrinsic depths greater than 1 per cent of the continuum were included in the line list over the full ESPaDOnS spectral range (370–1050 nm), resulting in 1648 He and metallic lines. The line list was further reduced by removing all intrinsically broad He and H lines, all lines that are blended with these lines, in addition to all lines blended with atmospheric telluric lines. This resulted in a final list of 571 metallic lines used to extract the final LSD profiles computed on a 1.8 km s^{-1} velocity grid, as illustrated in Fig. 2. The detection probability for each LSD spectrum was computed according to the criteria of Donati et al. (1997). Each observation resulted in a definite detection (DD) of an excess signal in Stokes V within the line profile [false alarm probability (FAP) <10^{-5}], except for the observations obtained on the nights of 2008 December 5 and 2009 May 7, which were non-detections (ND).

We calculated the longitudinal magnetic field (B_ℓ) and null measurements (N_ℓ) from each LSD profile using the first-order moment method discussed by Rees & Semel (1979), using an integration range between −25 and 75 km s^{-1} (see Table 1). This range was adopted to encompass the full profile range of the Stokes V signature. The resulting B_ℓ measurements range from −170 to −350 G with a median uncertainty of 20 G.

2.2 Spectroscopic data and measurements

In addition to the polarimetric spectra, we also utilized archival spectroscopic observations to analyse the line profile variability (LPV) of Hα. Seven spectra were obtained with the Coudé Auxiliary Telescope (CAT) using the Coudé Echelle Spectrograph

Table 1. Journal of polarimetric observations listing the date, the heliocentric Julian date (245 0000+), the number of subexposures and the exposure time per individual subexposure, the phase according to equation (1), the peak signal-to-noise ratio (S/N) (per $1.8\,\text{km}\,\text{s}^{-1}$ velocity bin) in the V band, the mean S/N in LSD Stokes V profile, the evaluation of the detection level of the Stokes V Zeeman signature according to Donati et al. (1997) (DD = definite detection, ND = no detection) and the derived longitudinal field and longitudinal field detection significance z from both V and N. The first seven observations were already discussed by Grunhut et al. (2009).

Date	HJD (245 0000+)	t_{exp} (s)	Phase	PK S/N	LSD S/N	Det. flag	$B_\ell \pm \sigma_B$ (G)	z	$N_\ell \pm \sigma_N$ (G)	z
2008-12-05	4806.0798	$1 \times 4 \times 500$	0.9408	311	2186	ND	354 ± 93	3.8	-59 ± 93	0.6
2008-12-06	4807.1081	$1 \times 4 \times 500$	0.9570	949	8339	DD	248 ± 24	10.3	-11 ± 24	0.5
2009-05-04	4955.7675	$1 \times 4 \times 540$	0.2955	1463	12 769	DD	-42 ± 17	2.5	-19 ± 17	1.1
2009-05-05	4956.7498	$2 \times 4 \times 600$	0.3109	1388	12 192	DD	-64 ± 18	3.6	-23 ± 18	1.3
2009-05-07	4958.7805	$2 \times 4 \times 540$	0.3429	653	5546	ND	-78 ± 39	2.0	-17 ± 39	0.4
2009-05-08	4959.7489	$1 \times 4 \times 540$	0.3581	1094	9515	DD	-153 ± 23	6.7	9 ± 23	0.4
2009-05-09	4960.7480	$2 \times 4 \times 540$	0.3738	900	7634	DD	-126 ± 29	4.4	-7 ± 29	0.2
2009-12-31	5197.0957	$2 \times 4 \times 540$	0.0917	1566	14 309	DD	233 ± 14	16.2	-7 ± 14	0.5
2010-01-03	5201.0427	$2 \times 4 \times 540$	0.1538	1110	10 354	DD	133 ± 20	6.6	-1 ± 20	0.0
2010-01-23	5219.9545	$2 \times 4 \times 540$	0.4512	1376	12 569	DD	-169 ± 18	9.6	-13 ± 18	0.8
2010-01-29	5225.9836	$2 \times 4 \times 540$	0.5461	1610	14 758	DD	-174 ± 15	11.5	12 ± 15	0.8
2010-01-31	5228.0015	$2 \times 4 \times 540$	0.5779	1179	10 817	DD	-172 ± 20	8.5	-33 ± 20	1.6
2010-02-01	5228.9032	$2 \times 4 \times 540$	0.5920	1250	8088	DD	-162 ± 27	6.0	-8 ± 27	0.3
2010-02-24	5251.9131	$2 \times 4 \times 414$	0.9540	1198	10 940	DD	234 ± 18	12.7	34 ± 18	1.9
2010-02-28	5255.9891	$2 \times 4 \times 414$	0.0181	932	7208	DD	190 ± 28	6.8	-33 ± 28	1.2
2010-03-04	5259.9420	$2 \times 4 \times 414$	0.0803	1163	10 477	DD	208 ± 20	10.6	-10 ± 20	0.5
2010-03-08	5263.9096	$2 \times 4 \times 414$	0.1427	878	7921	DD	187 ± 26	7.1	-4 ± 26	0.2
2010-11-28	5529.0352	$2 \times 4 \times 415$	0.3133	1224	10 980	DD	-60 ± 19	3.1	-5 ± 20	0.3
2010-12-24	5555.0639	$2 \times 4 \times 415$	0.7227	1083	9567	DD	-13 ± 22	0.6	-27 ± 22	1.2
2010-12-30	5561.0731	$2 \times 4 \times 415$	0.8172	995	8850	DD	89 ± 23	3.8	20 ± 23	0.9

(CES; $R \sim 45\,000$) at the European Southern Observatory (ESO), La Silla, Chile in 1996 February. These observations were obtained as part of a large monitoring campaign of bright O-type stars, as described by Kaper, Fullerton & Baade (1998). Eight spectra were obtained with the Ultraviolet and Visual Echelle Spectrograph (UVES; $R \sim 50\,000$) mounted on ESO's Very Large Telescope (VLT) on 2002 December 13. These spectra were combined to yield a single observation. Five spectra were obtained with the Fibre-fed Extended Range Optical Spectrograph (FEROS; $R \sim 48\,000$) mounted on ESO's 2.2-m telescope at La Silla: four observations between 2004 February 7 and 2004 February 10 (on three separate nights), and another observation on 2004 December 22. Between 2009 October 7 and 2009 October 9 ten spectra were obtained with the Echelle spectrograph ($R \sim 40\,000$) on the 2.5-m du Pont telescope at the Las Campanas Observatory (LCO). The nightly spectra were combined to produce three distinct observations. Lastly, we also used spectra from the Be Star Spectra (BeSS) data base obtained between 2008 November and 2011 April. 51 spectra were collected, primarily with a LHIRES3 spectrograph ($R \sim 15\,000$) using various telescopes with diameters between 0.2 and 0.3 m. A log of these spectroscopic observations is listed in Table 2.

From the spectroscopic data sets we measured the equivalent width (EW) variations of Hα (in addition to several additional spectral lines present in the ESPaDOnS data set – see Section 6 for further details), following the same procedure as described by Wade et al. (2012a). The Hα EW measurements are listed in Table 3.

We also utilized archival *International Ultraviolet Explorer* (*IUE*) spectra, the details of which are described by Grunhut et al. (2009).

2.3 Photometric data

Photometric observations were also utilized to study the optical variability (see Section 3) and to characterize the stellar and circumstellar emission properties (see Section 7.2).

The optical photometric time series corresponds to 85 measurements from *Hipparcos* (Perryman et al. 1997) collected on 64 different nights between 1990 April 3 and 1993 June 6.

Additional photometric observations used to construct the spectral energy distribution (SED) consists of optical data obtained from the Centre de Données astronomiques de Strasbourg (CDS), and infrared (IR) measurements from the Two Micron All Sky Survey (2MASS), the Deep Near Infrared Survey (DENIS), the *Infrared Astronomical Satellite* (*IRAS*), the *Akari* satellite and the *Wide-field Infrared Survey Explorer* (*WISE*), which were all obtained from NASA's Infrared Science Archive (IRSA). Additionally, we also used photometry from The, Wesselius & Janssen (1986).

The optical and IR magnitudes were converted to flux measurements at the zero-point of the associated photometric filters using conventional methods.

3 PERIOD ANALYSIS

Grunhut et al. (2009) attempted to infer the rotational period (P_{rot}) of HD 57682 based on the limited temporal sampling of their data set. With the larger data set presented in this paper, we re-evaluate the periodicity and rotation period of HD 57682.

Using a Lomb–Scargle technique (Press et al. 1996), we analysed the longitudinal magnetic field variations B_ℓ and the EW measurements of Hα. The periodograms obtained from these analyses are
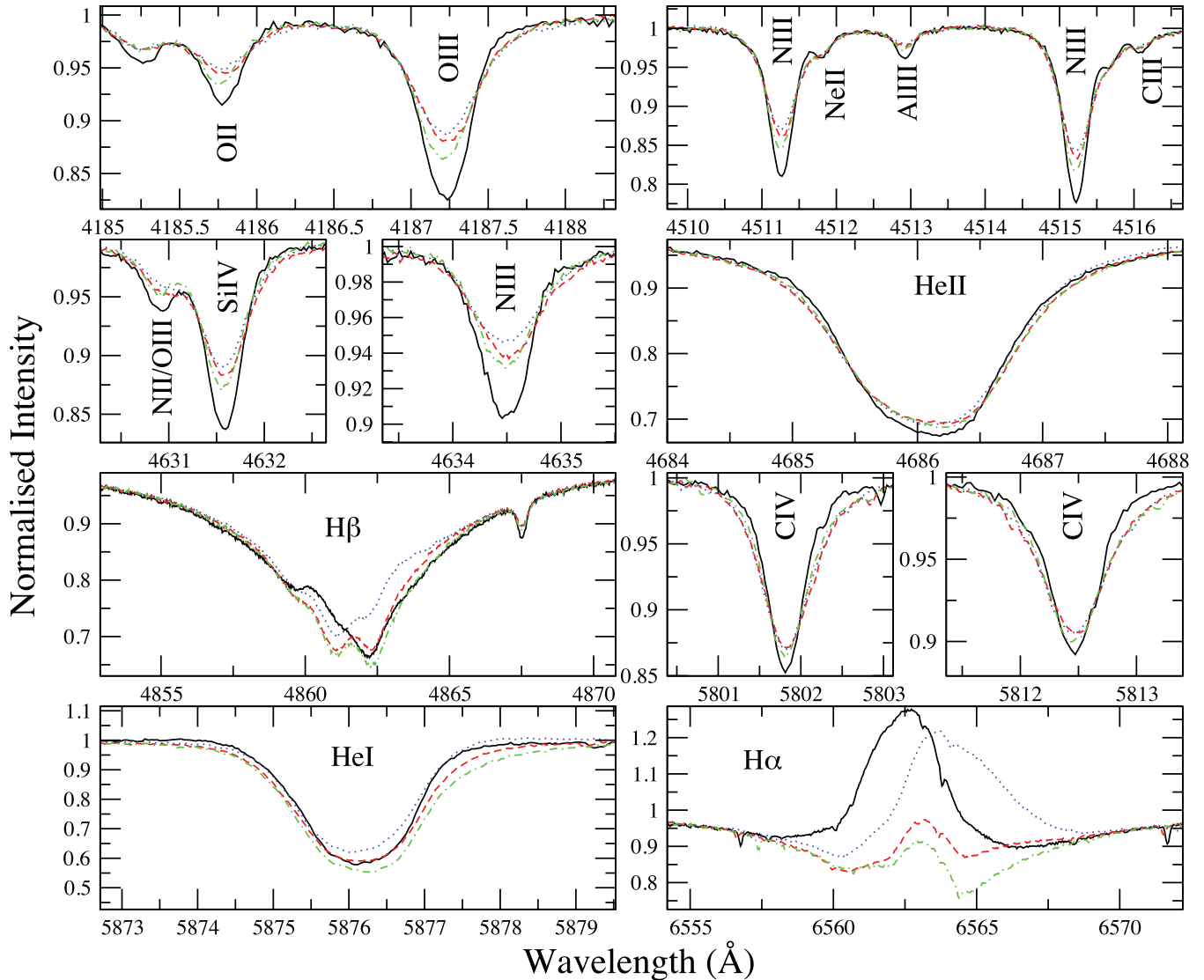
Figure 1. Selected regions of visible spectra from ESPaDOnS. Spectra at different rotational phases are shown to highlight the observed variability in almost all lines (0.02 – solid black, 0.30 – dashed red, 0.45 – dotted blue, 0.72 – dash–dotted green; see Section 6 for further details). The ions with the most significant contribution to each line are also labelled.

displayed in Fig. 3. The results obtained from the B_ℓ measurements show a clear peak in the periodogram at a period of $63.52^{+0.18}_{-0.17}$ d, where the uncertainties represent the 1σ limits. When phased with this period, the B_ℓ measurements show a clear sinusoidal variation. However, the periodogram obtained from the Hα measurements shows a clear peak occurring at $31.7929^{+0.0029}_{-0.0014}$ d, roughly half the period that is obtained from the B_ℓ measurements. If we phase the Hα EW measurements to this period, we obtain a roughly sinusoidal variation, but with a relatively broad dispersion. On the other hand, the B_ℓ measurements cannot be reasonably phased with this period. We proceeded to obtain a periodogram of the Hα data using the multiharmonic fitting technique of Schwarzenberg-Czerny (1996), including contributions from the first harmonic only. The resulting periodogram shows two peaks, one occurring at about 31 d and the other occurring at 63.5708 ± 0.0057 d. This second peak is consistent with the period found from the magnetic measurements. Therefore, adopting this period as the stellar rotation period and the phase of maximum positive B_ℓ as HJD_0 we derive the following

ephemeris:

$$HJD^{max}_{B_\ell} = 245\,3347.71(35) + 63.5708(57)\,E, \qquad (1)$$

where the uncertainties (1σ limits) in the last digits are indicated in brackets. Unless otherwise stated, all further data are phased according to this ephemeris.

In Fig. 4 we show the phased B_ℓ measurements, Hα EW variations, and *Hipparcos* photometry of HD 57682. The B_ℓ measurements follow a simple, sinusoidal variation with maximum positive B_ℓ occurring at phase 0.0 and maximum negative B_ℓ occurring at phase 0.5. The Hα EW measurements show a double-peaked variation with maximum emission occurring at phases 0.0 and 0.5, and minimum emission occurring at phases 0.25 and 0.75. This is further discussed in Section 7. The *Hipparcos* measurements do not show any significant variations when phased with the rotation period. Furthermore, the periodogram shows no significant power at this or any other period and the scatter of the photometric variations and their associated uncertainty is fully consistent with no variability.
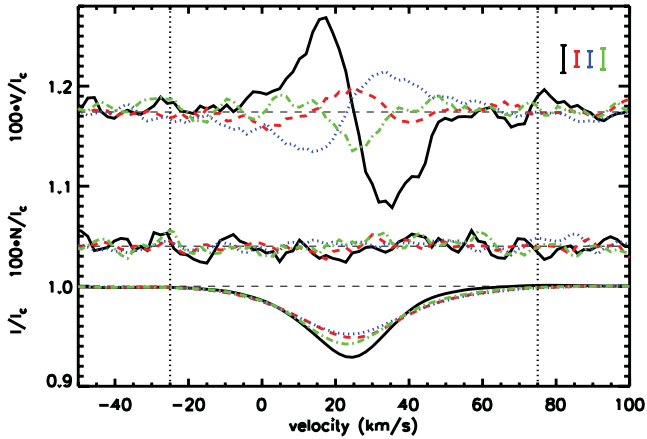
Figure 2. Mean LSD Stokes V (top), diagnostic null (middle) and Stokes I profiles (bottom) of HD 57682 from observations obtained at four different rotational phases (see Section 3; 0.02 – solid black, 0.30 – dashed red, 0.45 – dotted blue, 0.72 – dash–dotted green). The V and N profiles are expanded by the indicated factor and shifted upwards, and smoothed with a 3-pixel boxcar for display purposes. A clear Zeeman signature is detected at most phases in the Stokes V profiles, while the null profile shows no signal. The integration limits used to measure the longitudinal field are indicated by the dotted lines and the mean 1σ pixel uncertainty for each profile is also shown.

Table 2. Journal of spectroscopic observations listing the identification of the data set, the typical resolving power of the instrument, the epoch of the observations, the number of spectra obtained within the given data set, the resulting number of distinct observations and the median per pixel S/N in the Hα region for the data set.

Name	Res. power	Epoch	Num spec	Num obs	Median S/N
CES	45 000	1996	7	7	540
UVES	50 000	2002	8	1	160
FEROS	48 000	2004	5	5	170
LCO	40 000	2009	10	3	360
BeSS	15 000	2008–2011	51	51	70

Table 3. Spectroscopic Hα EW measurements. Included is the instrument or observatory name, the heliocentric Julian date and the measured Hα EW and its corresponding 1σ uncertainty. Shown here is only a sample of the table. The full table can be found in Appendix A.

Data set	HJD	Hα EW (Å)	σ_{EW} (Å)
CES	245 0125.6216	1.270	0.014
CES	245 0126.6291	1.108	0.007
CES	245 0127.6296	0.926	0.008
CES	245 0128.6284	0.735	0.012
CES	245 0129.6287	0.569	0.011
CES	245 0130.6194	0.454	0.010

4 ROTATIONAL BROADENING

Grunhut et al. (2009) measured the projected rotational velocity ($v \sin i$) using the Fourier transform method (e.g. Gray 1981; Jankov 1995; Simón-Díaz & Herrero 2007). They compared the positions of the first nodes in the Fourier spectrum to a theoretical Gaussian profile convolved with a rotationally broadened profile corresponding to a particular $v \sin i$, and found a $v \sin i = 15 \pm 3 \, \text{km s}^{-1}$.

If we assume rigid rotation and take the radius as inferred by Grunhut et al. (2009) ($R_\star = 7.0^{+2.4}_{-1.8} \, \text{R}_\odot$) and the period obtained in this work ($P = 63.5708 \, \text{d}$), we find a maximum allowed $v \sin i$ (i.e. for $\sin i = 1$) $\sim 7.5 \, \text{km s}^{-1}$, which is inconsistent with the results obtained from the Fourier analysis. This implies that contributions from non-rotational broadening, as noted by Grunhut et al. (2009), significantly affect the Fourier spectrum resulting in the incorrect interpretation of the first node representing the rotational broadening.

In our endeavour to constrain the rotational broadening, we reanalysed the spectra, particularly focusing on those obtained at phases where the lines appeared their narrowest and therefore were least affected by macroturbulence (see Section 6 for further details). We identified lines from a theoretical SYNTH3 (Kochukhov 2007) spectrum for which the resulting Fourier spectrum was minimally affected when significant contributions of macroturbulence were included. We then compared the Fourier spectrum obtained from a theoretical profile with $5 \, \text{km s}^{-1}$ rotational broadening to that obtained from the observed spectrum and measured the difference between the positions of the first nodes to obtain the $v \sin i$ of the spectral line. Using this procedure on several lines from the spectrum obtained on 2009 December 31 indicate a $v \sin i = 6.1 \pm 1.9 \, \text{km s}^{-1}$, consistent with the range implied by the rotation period and estimated radius of HD 57682. However, we note that this period is sufficiently imprecise that it cannot be used to usefully constrain the inclination of the rotation axis. We also found that the C IV $\lambda 5801$ line was one of the lines least affected by the addition of macroturbulence and therefore also used this single line to determine a unique $v \sin i$, as illustrated in Fig. 5. From measurements of this line at several rotation phases we find a best-fitting $v \sin i = 4.6 \pm 0.6 \, \text{km s}^{-1}$, where the uncertainties represent the 1σ limits. Given the range of $v \sin i$ obtained from the C IV $\lambda 5801$, our adopted $R_\star$ and P_{rot}, implies that $i \sim 56^{\circ +35^\circ}_{-23^\circ}$, or that we can place a lower limit on i such that $i > 30^\circ$, at a 1σ confidence. However, at $\sim 4.6 \, \text{km s}^{-1}$ we are approaching the spectral resolution of ES-PaDOnS ($\sim 4.4 \, \text{km s}^{-1}$) and therefore one must be cautious to not overinterpret these results.

5 MAGNETIC FIELD GEOMETRY

The magnetic field geometry of HD 57682 was investigated assuming the field is well described by the oblique rotator model (ORM), which is characterized by four parameters: the phase of closest approach of the magnetic pole to the line-of-sight ϕ_0; the inclination of the stellar rotation axis i; the obliquity angle between the magnetic axis and the rotation axis β and the dipole polar strength B_d. This model naturally predicts the simple sinusoidal variation of the longitudinal magnetic field measurements as shown in Fig. 4, implying that the longitudinal field curve of HD 57682 is well described by a simple dipole topology of its global magnetic field.

We first attempted to infer the characteristics of the magnetic field based on the B_ℓ measurements. These measurements are nearly symmetric about 0 and we can therefore infer that either i or β (or both) are close to 90°. This is similar to the B_ℓ variation of β Cephei (e.g. Donati et al. 2001), and similar to this star, B_d and β are well constrained except as i approaches 0° or 90°. As i approaches 0°, B_d becomes unconstrained, while as i approaches 90°, β becomes unconstrained. To infer the characteristics of the magnetic field, we carried out a χ^2 minimization, comparing the observed B_ℓ curve to a grid of computed longitudinal field curves to determine B_d and β for a fixed linear limb darkening coefficient of 0.35 (Claret 2000) and various fixed inclinations.
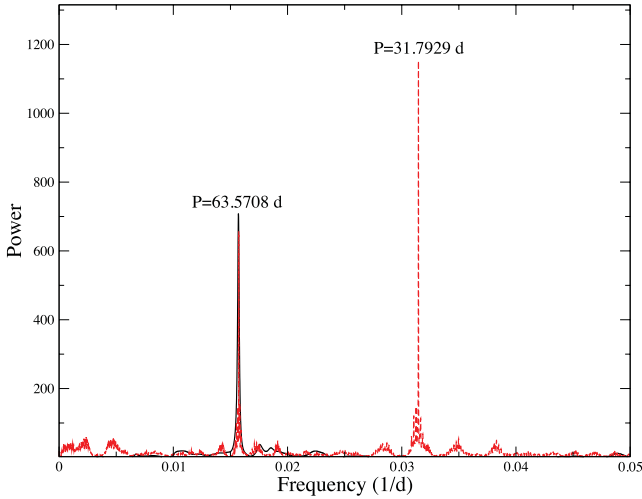
Figure 3. Periodograms obtained from the B_ℓ measurements (solid black) and from the Hα EW variations including contributions from the first harmonic (dashed red). Note the strong power present in the Hα periodogram at $P = 31.7927$ d but the lack of power from the B_ℓ measurements at this period. However, a consistent period is found at $P = 63.5708$ d from both data sets.

The resulting χ^2 distributions from our fits are shown in Fig. 6. For an assumed $i = 60°$ we find that $B_d = 880 \pm 50$ G and $\beta = 79° \pm 4°$. If we take $i = 30°$, we infer that $B_d = 1500 \pm 90$ G and $\beta = 86° \pm 2°$, which places an upper limit on the dipole field strength if $i > 30°$ as implied from the constraints derived in Section 4. Also shown in Fig. 6 are χ^2 distribution for other inclinations to illustrate how the distribution varies as a function of inclination.

We also attempted to constrain the magnetic field characteristics based on fits to the individual LSD Stokes V profiles by comparing our profiles to a large grid of synthetic profiles, also characterized by the ORM. The models were computed by performing a disc
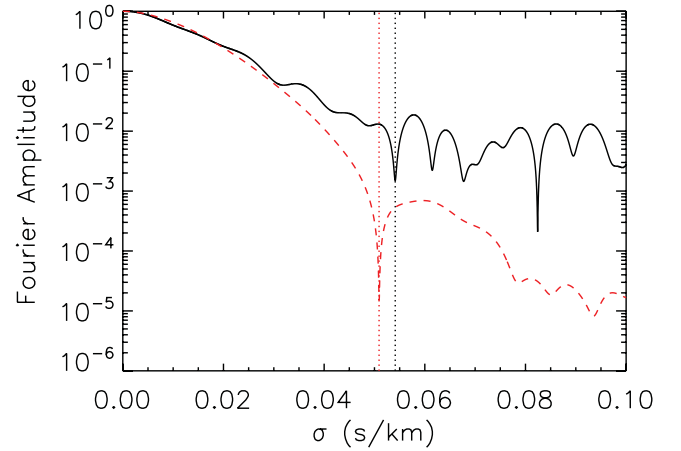

Figure 5. Fourier spectrum of the C IV $\lambda 5801$ line solid black compared to a theoretical line profile with $v \sin i = 5$ km s^{-1} with an additional macroturbulent velocity of 20 km s^{-1} dashed red, which we find necessary to provide a good fit to the observed line profile. The difference in the positions of the first nodes (as indicated by the vertical dotted lines) is used to determine the best-fitting $v \sin i = 4.2$ km s^{-1} for this observation.

integration of local Stokes V profiles assuming the weak field approximation and uniform surface abundance. The parameters of the Stokes V profiles were chosen to provide the best fit to the width of the average of all the observed I profiles, and the best fit to the depths of each individual observed I profile. For each observation we found the parameters that provided the lowest χ^2 value and inferred the maximum likelihood by combining these results in a Bayesian framework.

We conducted our fits for varying inclinations and found that the maximum likelihood model for $i \sim 80°$ provided the lowest combined total χ^2, but this value was not significantly different from those obtained for other inclinations. However, as i increased we did find increasing deviations between the best B_ℓ-fit and
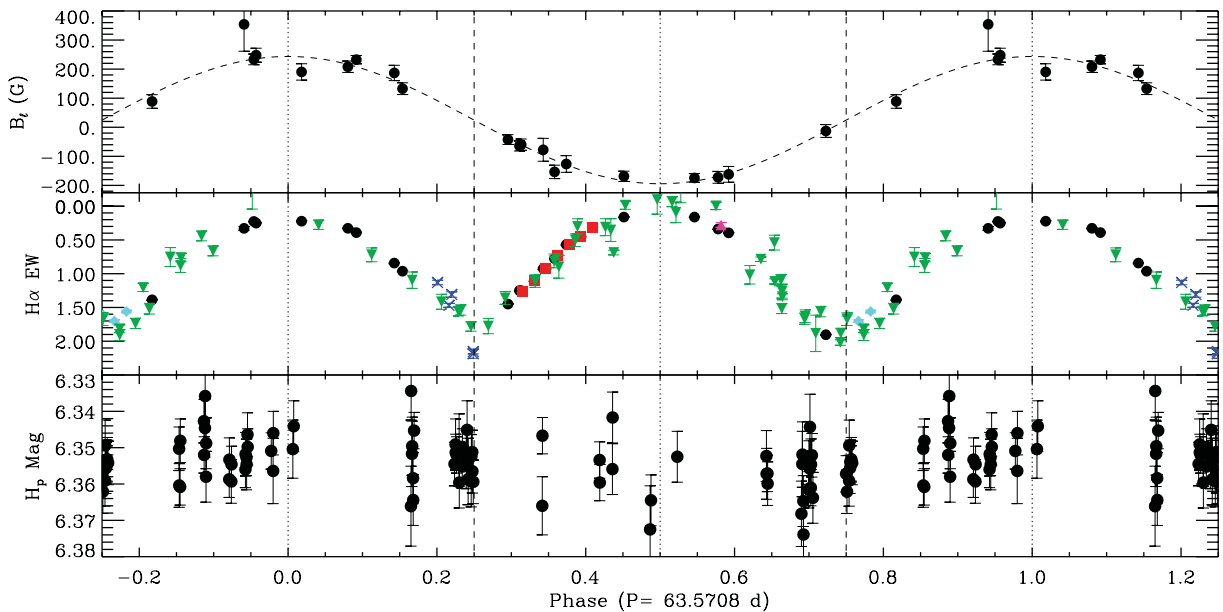
Figure 4. Phased observational data using the ephemeris of equation (1). Upper: longitudinal magnetic field variations measured from LSD profiles of the ESPaDOnS spectra. Middle: Hα EW variations measured from ESPaDOnS (black circles), CES (red squares), FEROS (blue Xs), Las Campanas Observatory (turquoise diamonds), UVES (pink up-facing triangles) and BeSS (green down-facing triangles) data sets. Lower: *Hipparcos* photometry. The dashed curve in the upper frame represents a least-squares sinusoidal fit to the data.
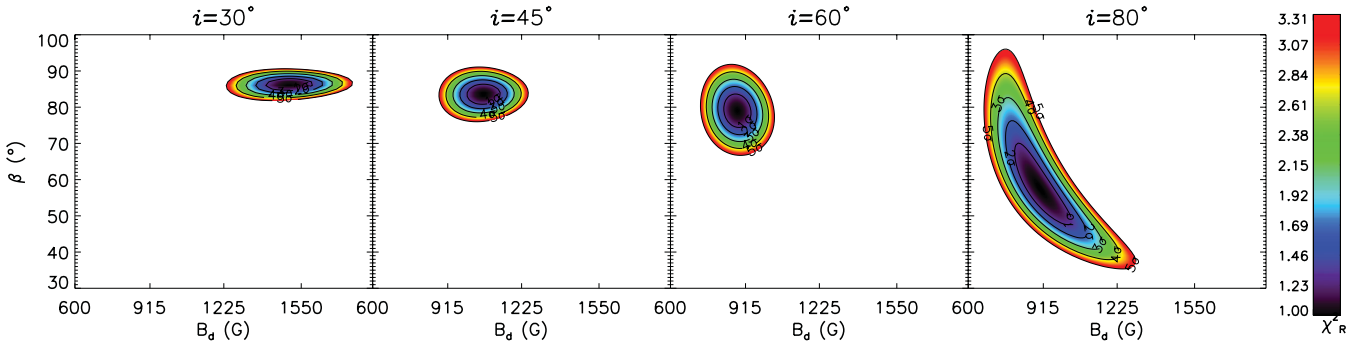
Figure 6. Reduced χ^2 contours of dipole field strength B_d versus magnetic obliquity β permitted by the longitudinal field variation of HD 57682 for varying inclinations.

profile-fit model parameters; at $i = 30°$ we found a best B_ℓ-fit $\beta = 86°$ and a profile-fit $\beta = 80°$; at $i = 80°$ we found a best B_ℓ-fit $\beta = 56°$ but $\beta = 34°$ from the profile fits. We therefore conclude that we are unable to constrain the inclination from fits to the LSD profiles and continue to adopt $i = 60°$ for the remainder of this discussion as this is the inclination inferred from the $v \sin i$ measurements and provides similar magnetic parameters from both the B_ℓ and profile fits.

The maximum likelihood profile-fit model for $i = 60°$ was found with $B_d = 700 \pm 30$ G, where the uncertainty corresponds to the 95.6 per cent significance level, and $\beta = 68° \pm 2°$, with the uncertainty corresponding to the 98.2 per cent confidence limits. While the formal uncertainties are very low, we note that individual best-fitting parameters to each observation range from $B_d \sim 400$–2000 G to $\beta \sim 0°$–150°. However, while the fits to B_d and β are not well constrained from fits to the individual observations at most phases, the maximum likelihood model is well constrained.

In Fig. 7 we compare the observed Stokes *V* profiles (grey circles) with the best profile-fit model for the given observation (dash–dotted blue), the maximum likelihood LSD model (dotted red) and the model corresponding to the best-fitting parameters that were obtained from the B_ℓ measurements for $i = 60°$ ($B_d = 880$ G and $\beta = 79°$; solid green). The quality of the fits of the best-fitting and maximum likelihood models is similar, which shows that a single dipole configuration can reasonably reproduce the observed Stokes *V* profiles. However, systematic differences, particularly in the wings of the profiles, are evident between the models and the observations, resulting from the fact that our simple model cannot reproduce the extended wings in the observed *I* or *V* profiles. It is also evident that the model corresponding to the best fit to the B_ℓ curve does a poorer job of fitting the observed Stokes *V* profiles at several phases, possibly indicating that there may be an issue with the way we chose to model the line profiles.

We investigated this potential issue by re-conducting our fits, but neglecting the varying line depths for each observation as was done in the original procedure. Instead we adopted a line depth as determined from the average of all our observations. From the new fits for $i = 60°$ we found a best-fitting $B_d \sim 900$ G, which is consistent with the results of the B_ℓ measurements. However, we find a larger disagreement between the inferred magnetic obliquity as β was found to be $\sim 60°$. We also note that the overall combined total χ^2 value was slightly worse from these fits.

Another possibility is that the global magnetic topology contains significant contributions from higher order multipoles. The B_ℓ curve is rather insensitive to these higher order moments, in contrast to the velocity-resolved Stokes *V* profiles. We investigated this possi-

bility by applying our fitting procedure to a time series of synthetic profiles calculated assuming our original dipole, supplemented by a significant aligned quadrupolar field moment. This model yields a longitudinal field curve essentially indistinguishable from that produced by the pure dipole. Our tests indicate that by trying to fit a pure dipole model to the dipole+quadrupole profiles, the procedure would systematically infer dipole field strengths that were strongly incompatible with the results obtained from the B_ℓ curve. Specifically, our tests showed a systematic overestimation of the dipole field strength at most phases. This trend is inconsistent with the measurements presented in Fig. 7 and we therefore conclude that our polarimetric observations do not suggest any significant detectable contributions from higher order multipoles.

6 LINE VARIABILITY

## 6.1 Equivalent width and radial velocity measurements

HD 57682 stands out from the sample of magnetic O-type stars due to its sharp spectral lines and the apparently limited contamination of its spectrum by wind and circumstellar plasma emission. Detection and measurement of the line profile variations (e.g. Stahl et al. 1996) can therefore be performed more sensitively for a much larger sample of lines than for any other magnetic O-type star. It therefore represents a uniquely suited target for understanding the general influence of magnetized winds of O-type stars on their spectrum and spectral variability.

To quantify the variability, we used the EW variations for numerous spectral lines. We also measured the radial velocities of each spectral line by fitting a Gaussian to the cores of the profiles to determine the central wavelength at each phase. A number of other methods were investigated, but we ultimately settled on fitting the cores using a Gaussian as it provided less scatter in the measurements. However, since Hα displayed too much emission to carry out this fitting, we quantified the radial velocity of Hα by measuring the centre of gravity (or centroid) of the line profile.

Our observations reveal that HD 57682 displays a rich variety of line profile variability. In addition to the double-wave variations of the Hα line discussed in Section 3, we observe variations in essentially every line present in the stellar spectrum, including other H Balmer lines, lines of neutral and ionized He and lines of metals: C III and C IV, N III, O II, Mg II and Si III and Si IV. The EW and radial velocities of all lines vary coherently when phased according to the rotational ephemeris (equation 1).

The line variations can be approximately grouped into two categories. The first represents lines (mostly metals and some neutral
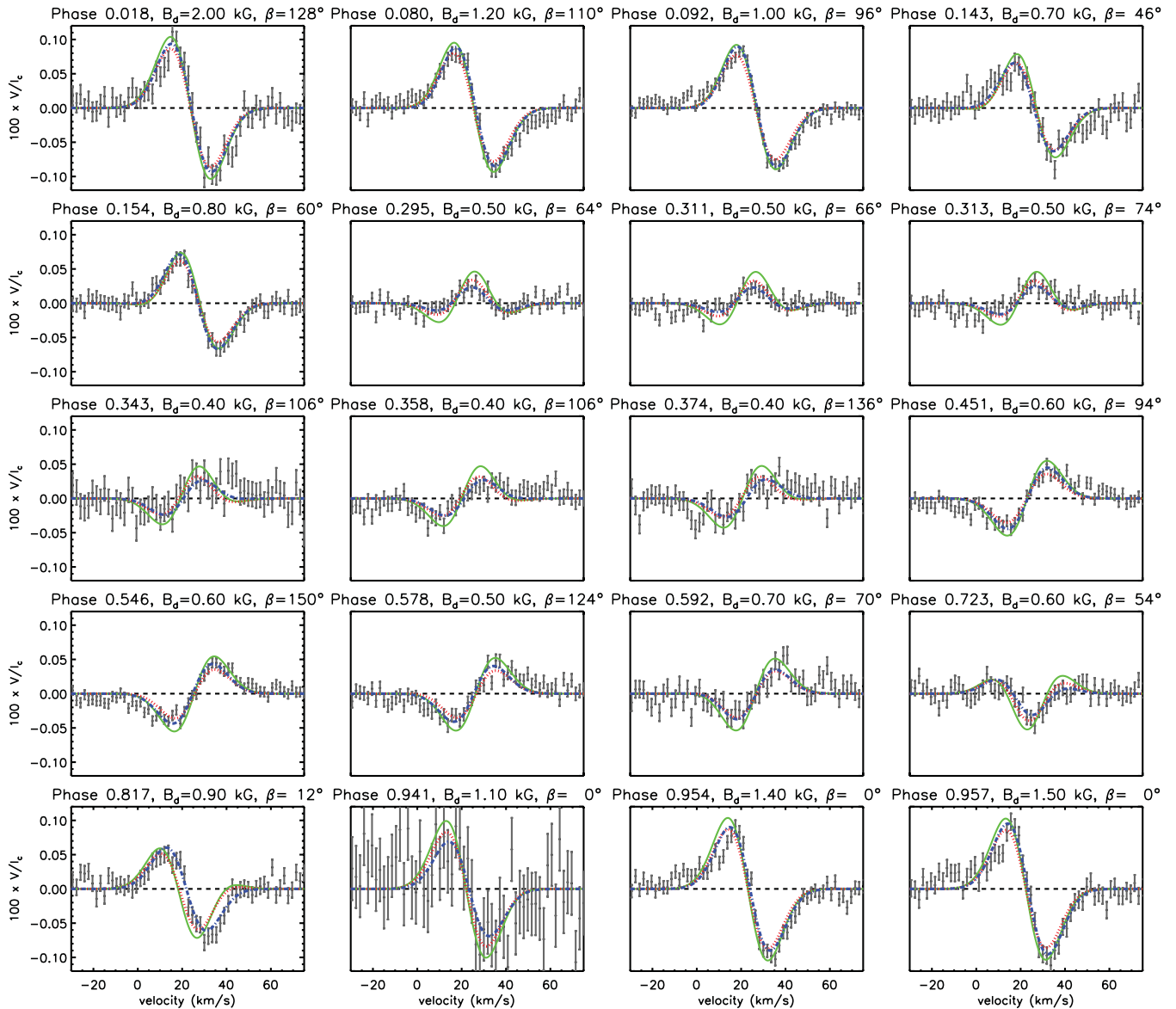
Figure 7. Mean circularly polarized LSD Stokes V profiles (grey circles). The error bars represent the 1σ uncertainties of each pixel. Also shown are the individual best-fitting model profiles for each phase (dash–dotted blue), the model that provides the global maximum likelihood (dotted red; $B_d = 700$ G, $\beta = 68°$) and the model corresponding to the best fit to the B_ℓ measurements ($B_d = 880$ G, $\beta = 79°$; solid green), all for an assumed inclination of $60°$. The phase and best-fitting parameters of the individual observations are also indicated.

He lines) with EW measurements that vary sinusoidally, as displayed in Fig. 8. The second includes those, like Hα, that display EW phase variations that are distinctly non-sinusoidal (as shown in Fig. 9), and likely directly reflect, to varying degrees, the variable projection of the flattened equatorial magnetospheric plasma density enhancement, as further discussed in Section 7. These groups are discussed in more detail below.

Except for C IV $\lambda\lambda5801$, 5812, all lines with sinusoidally varying EW measurements show minimum emission (or maximum absorption) at about phase 0.0 and maximum emission (or minimum absorption) at phase 0.5. At phase 0.5, these lines are shallower and broader than at phase 0.0, as illustrated in Fig. 1. The difference in line width and depth is quite significant. Most lines have an extended red wing at phase 0.5 that disappears at phase 0.0.

The Hα line shows variable emission with two maxima per rotation cycle. The phases of the emission extrema, 0.0 and 0.5, cor-

respond to the phases of longitudinal magnetic field extrema and therefore closest approach of the magnetic poles to the line-of-sight. In addition, the Hα EW curve exhibits two emission minima at phases 0.25 and 0.75, corresponding to the phases where the magnetic equator crosses the line-of-sight. These phenomena are usually interpreted (e.g. Donati et al. 2001) as the consequence of the variable projection of a flattened distribution of magnetospheric plasma trapped in closed loops near the magnetic equatorial plane, and possibly the occultation of the stellar disc by this plasma at phases 0.25 and 0.75. Only three other lines – He I $\lambda5876$, He II $\lambda4686$ and Hβ (see Fig. 9) – show clear evidence of similar reversals at phases 0.25 and 0.75, although a marginal contribution is suspected for He I $\lambda4921$ and He I $\lambda4471$. The emission level in Hα at phase 0.5 is roughly 10 per cent larger than at phase 0.0. Likewise, the emission minimum at phase 0.75 appears 20 per cent less than the corresponding emission minimum at phase 0.25. However, these
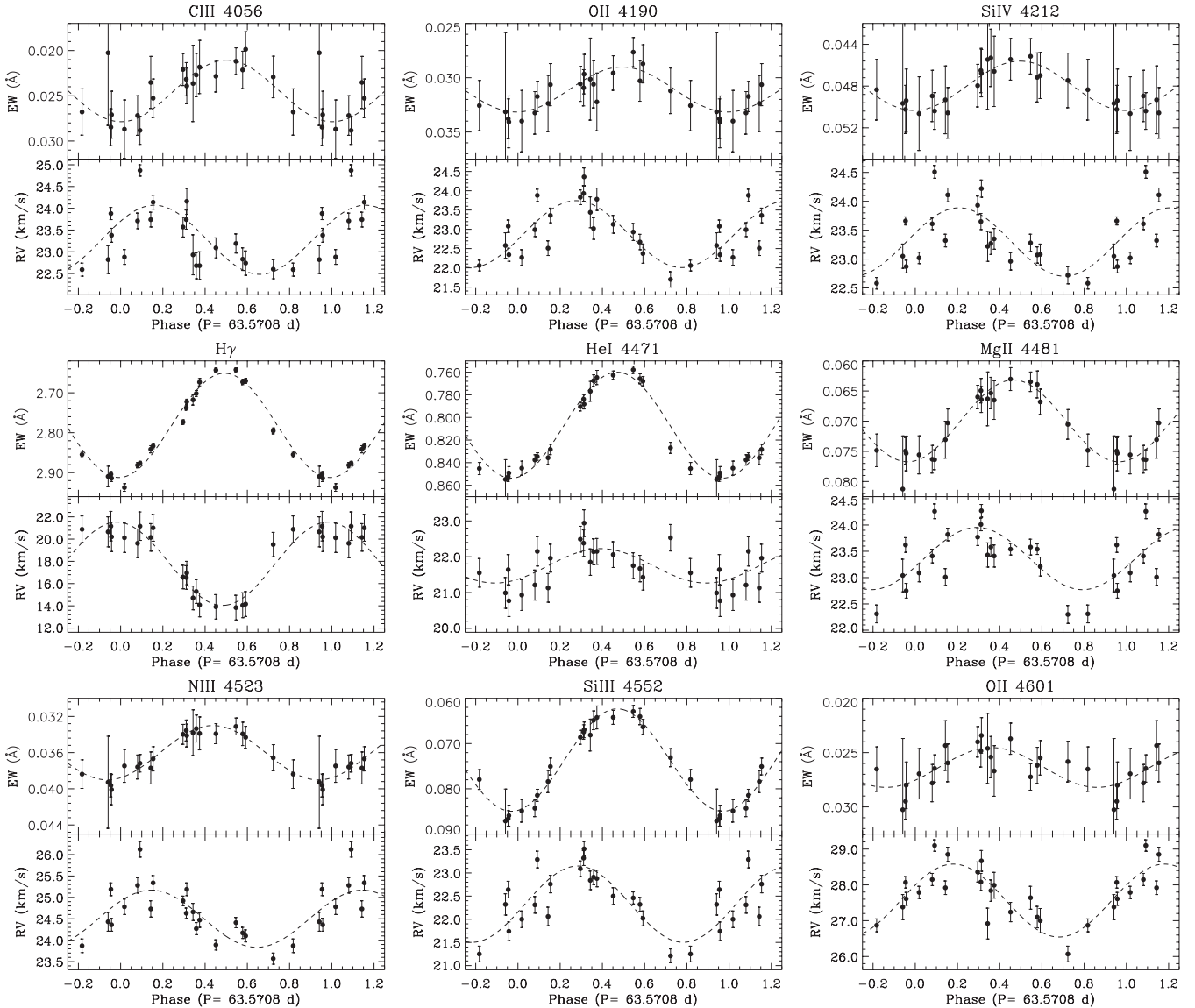
Figure 8. Rotationally phased EW measurements (top panels) and radial velocity measurements (bottom panels) for selected spectral absorption lines that appear to have sinusoidally varying EW measurements. Note that while the EW variations of Hγ are consistent with the other lines, the radial velocity variations are out of phase with the rest of the lines. Least-squares sinusoidal fits to the data are also shown (dashed curves).

measurements are primarily measured from BeSS spectra with limited S/N.

In almost all the spectral lines that show sinusoidally varying phased EW measurements, we find approximately sinusoidally varying radial velocity measurements. These variations reach a maximum radial velocity between phases 0.2 and 0.3 and show a peak-to-peak amplitude of about $2\,\mathrm{km\,s^{-1}}$, with a mean radial velocity of $\sim 22\,\mathrm{km\,s^{-1}}$. This is not the case for Hγ, which reaches a maximum radial velocity at phase 0.0 and minimum at phase 0.5, and shows a peak-to-peak difference of $\sim 8\,\mathrm{km\,s^{-1}}$. Other than Hβ, we see non-sinusoidal variations in the radial velocity measurements for the lines that show clear, non-sinusoidal EW variations, which often mirror the EW variations with maximum radial velocity occurring at minimum emission and minimum radial velocity occurring at maximum emission. The radial velocity measurements for Hβ phase in a similar manner with Hγ – they are nearly sinusoidal, reach maximum radial velocity at phase 0.0 and appear flat-topped.

6.2 Line profile variations

In Figs 10 and 11 we plot the phased line profile variations, or dynamic spectra. In these figures, we have subtracted the profile obtained on 2010 December 24 to highlight the variability. This spectrum was obtained at phase 0.72 and corresponds to the observation where the magnetic equator is passing our line-of-sight and, as previously discussed, when the flattened distribution of magnetospheric plasma is viewed nearly edge-on, and therefore provides the lowest contribution of emission. Our dynamic spectra indicate that a single pseudo-emission feature (a feature that appears in emission relative to the 2010 December 24 profile) occurs once per cycle, and is centred at phase 0.5 in the dynamic spectra of the lines with sinusoidally varying EW measurements (Fig. 10). In almost all these lines, we find that the pseudo-emission is mostly confined to the inner core region and extends further out in the blue wing than the red wing. During phases of maximum emission we also find increased pseudo-absorption in the red wing, except for He I λ4471, which
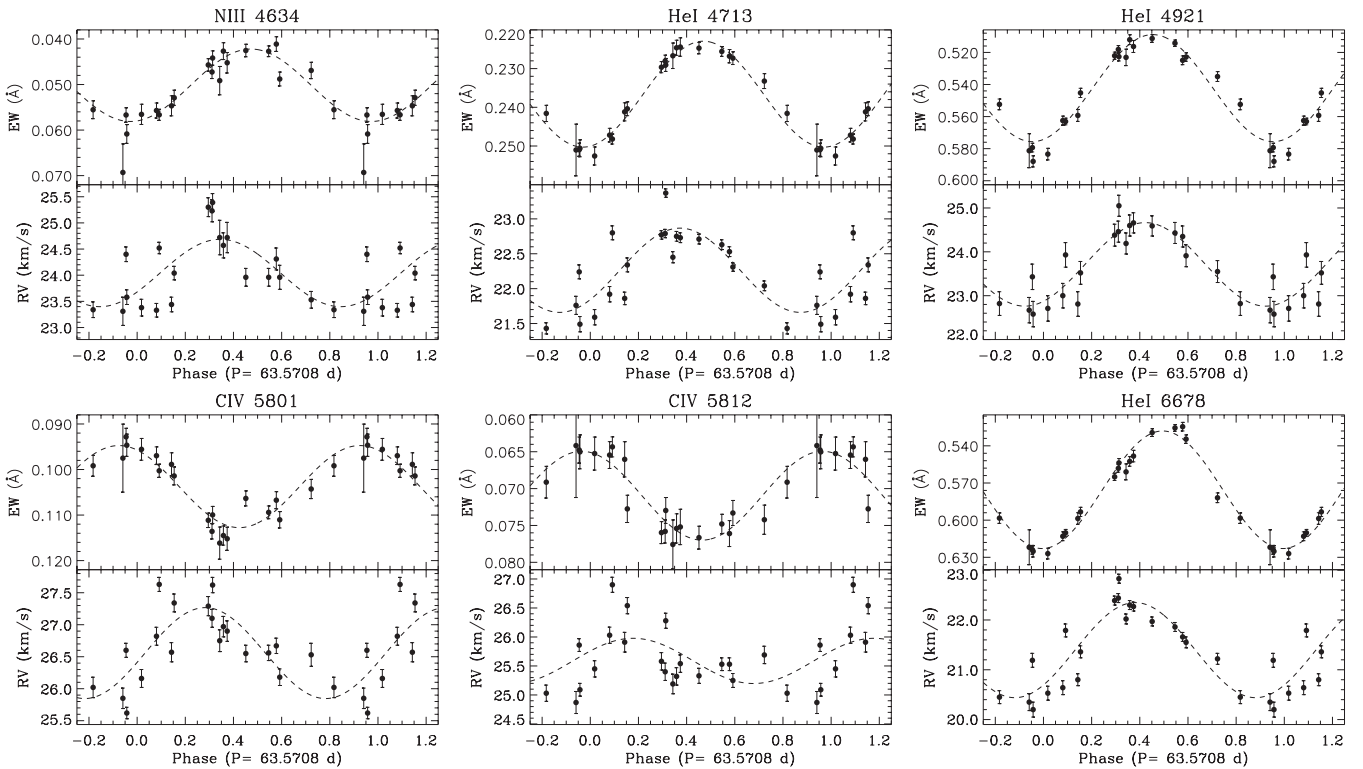
Figure 8 – *continued*

does not appear to show additional pseudo-absorption, but does show strong evidence of pseudo-emission during phases of maximum absorption, which is centred at phase 0.0. Other lines show varying amounts of pseudo-emission during this phase as well, but this feature is most prominent in the He lines shown in Fig. 10.

The dynamic spectra for the C IV lines appear different. Maximum emission still occurs once per cycle, centred at phase 0.5, but the emission feature is mainly constrained to the inner core region and does not extend into the blue wing as it does for other lines. During phases of maximum emission, there appears to be an increase in pseudo-absorption in both wings, but the absorption in the red wing appears stronger. A similar dynamic spectrum is also found for the He II λ4686 line, as shown in the left-hand panel of Fig. 11. In almost all the lines shown in Figs 10 and 11 we find that the features all appear at low velocities with the centres of the features increasing in velocity with increasing phase. However, this does not appear to be the case with the He lines, which appear more symmetric, except for the extended pseudo-absorption into the blue wing, which is likely caused by the forbidden transitions in these He lines.

In Fig. 12 we show the dynamic spectra of the other lines with non-sinusoidally varying EW variations. A non-local thermodynamic equilibrium (NLTE) TLUSTY (Lanz & Hubeny 2003) synthetic profile was subtracted from the Balmer lines in this figure to highlight the circumstellar emission contribution. As was found in the EW variations, we see two emission features per rotation cycle, one centred around phase 0.0 and the other centred around phase 0.5. In the He I λ5876, Hγ and Hβ line we find the lines to be mainly in absorption and the emission feature at phase 0.0 to be narrower and weaker in emission than the feature at phase 0.5. In the He I line shown, both emission features appear redshifted with respect to the systemic velocity of HD 57682; the narrower feature is found to have a central velocity of ∼75 km s^{-1} while the broader feature has a central velocity of ∼65 km s^{-1}. There also appears to be an

additional weak emission feature that is blueshifted with respect to the systemic velocity occurring at phase 0.0. Hβ and Hγ appear similar to the He I λ5876 line. Both show a strong and broad emission feature at phase 0.5, and a weaker, narrower emission feature at phase 0.0. This is not the case for Hα, which shows both emission features with nearly the same width and same emission level; it is evident that the strength of the weaker emission feature at phase 0.0 is decreasing for higher Balmer lines. Unlike the He I λ5876 line, the emission features of the Balmer lines have their central velocities alternating about the systemic velocity; the feature at phase 0.0 appears blueshifted, while the feature at phase 0.5 is redshifted.

7 CIRCUMSTELLAR ENVIRONMENT

7.1 Magnetosphere

As discussed in the previous section, the Hα emission variation is often qualitatively attributed to the variable projection of a flattened distribution of magnetospheric plasma trapped in closed loops near the magnetic equatorial plane. To this end, we explored the potential of using a 'Toy' model, similar to that described by Howarth et al. (2007), to fit the observed Hα EW variations. This model assumes that the Hα emission is formed in a centred, tilted, infinitely thin, optically thick disc, in which the relative emission is only a function of the projected area of the disc, taking into account occultation by the star. We are only able to model the relative emission, but our model indicates that if we assume the inclination angle between the disc axis and the rotation axis (α) is the same as the magnetic obliquity (β) then only subtle variations are predicted in the EW curve for different inclinations (assuming the relationship between i and β is constrained by the ORM), which are indistinguishable with the precision of our current measurements. We also find that higher α values provide much better fits and therefore we adopt
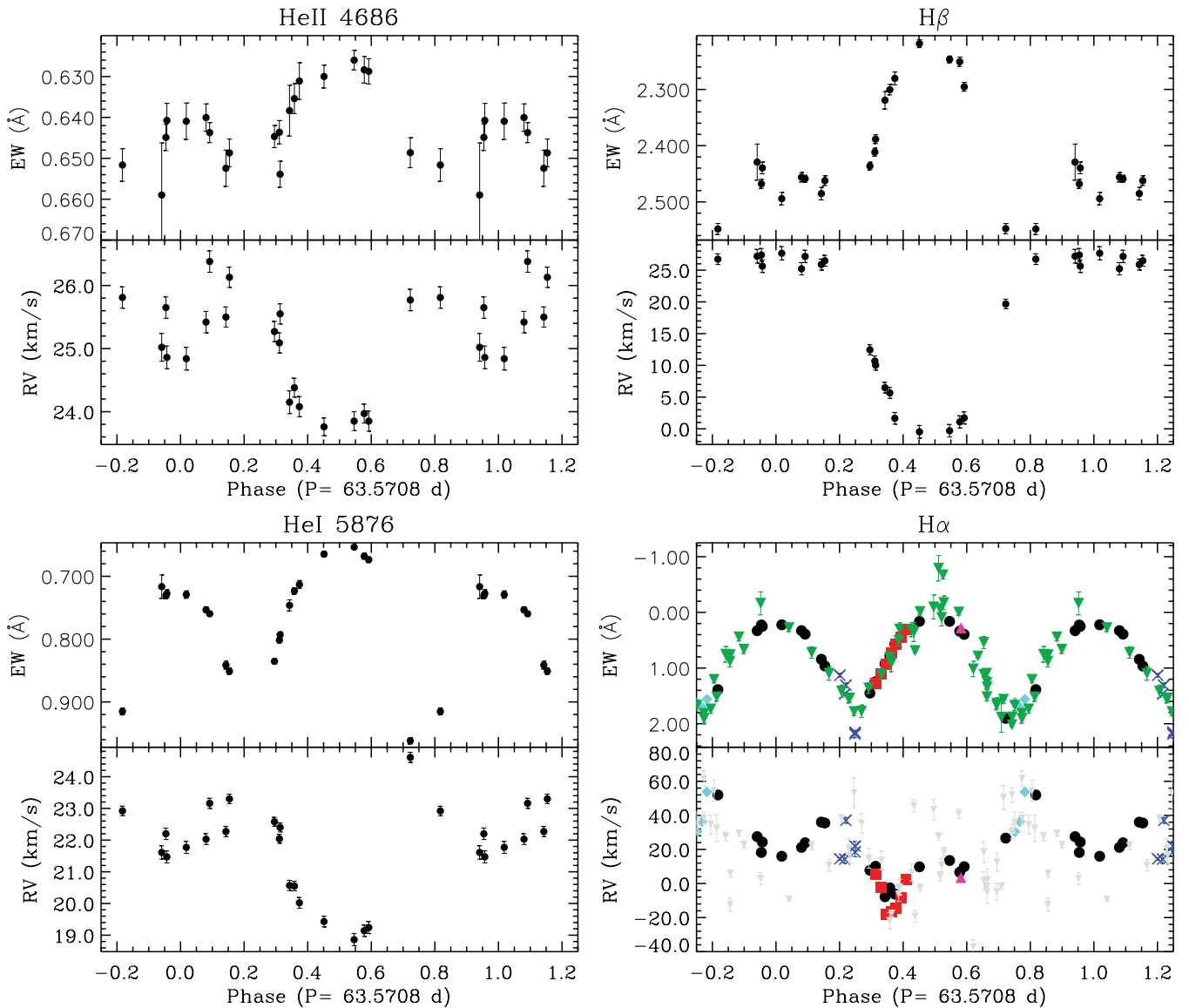
Figure 9. Rotationally phased EW measurements (top panels) and radial velocity measurements (bottom panels) for selected spectral absorption lines with clearly non-sinusoidal EW variations. Hα measurements from ESPaDOnS (black circles), CES (red squares), FEROS (blue Xs), Las Campanas Observatory (turquoise diamonds), UVES (pink up-facing triangles) and BeSS (green down-facing triangles) data sets. The BeSS Hα radial velocity measurements are shown as grey triangles. The large scatter of these measurements with respect to the other data sets likely results from their poor S/N and low spectral resolution.

the $\alpha = \beta = 79°$ as derived from the B_ℓ measurements as our disc inclination. Using this value, we first attempted to constrain the disc radii but realized that the inner (R_{in}) and outer (R_{out}) radii of the disc are poorly constrained by the precision of our observations. However, a best-fitting $R_{in} = 1.3 \pm 0.3\,R_\star$ and $R_{out} = 1.8^{+0.3}_{-0.2}\,R_\star$ (as measured from the centre of the star, i.e. a distance of $0.3 \pm 0.3\,R_\star$ and $0.8^{+0.3}_{-0.2}\,R_\star$ from the stellar surface) are found, where the uncertainties represent the 1σ limits. An illustration of this model is presented in Fig. 13.

A comparison between the predicted EW variations from our 'Toy' model and the observed EW variations is shown in Fig. 14. As illustrated, the model is able to qualitatively reproduce the general features of the observed EW variations including the sharp emission minima, the smooth variation during maximum emission and the double-peaked nature of the variability, suggesting that the Hα emission does form in an optically thick, flattened distribution

of circumstellar plasma with a disc-like structure. However, our model predicts a lower emission level between phases 0.0–0.25 and 0.75–1.0 and a higher emission level between phases 0.25–0.4 and 0.6–0.75 than observed, and there is a visible offset between the phases of emission minima; our model predicts the minima to occur at phases 0.23 and 0.77, not 0.25 and 0.75 as observed. To investigate these discrepancies, we conducted another search allowing the disc axis inclination to vary. Our results show that $\alpha = 88° \pm 1°$ (and a corresponding $R_{in} = 1.0\,R_\star$ and $R_{out} = 1.6\,R_\star$) provides a better overall fit to the observations, but is inconsistent with our derived value of β. This disc orientation is better able to reproduce the emission level throughout the rotation cycle and correctly predicts the phases of minimum emission as illustrated in Fig. 14.

In addition to investigating the magnetospheric properties via the 'Toy' model, we also used the method of Sundqvist et al. (2012) to study the Hα variability. Sundqvist et al. (2012) showed that
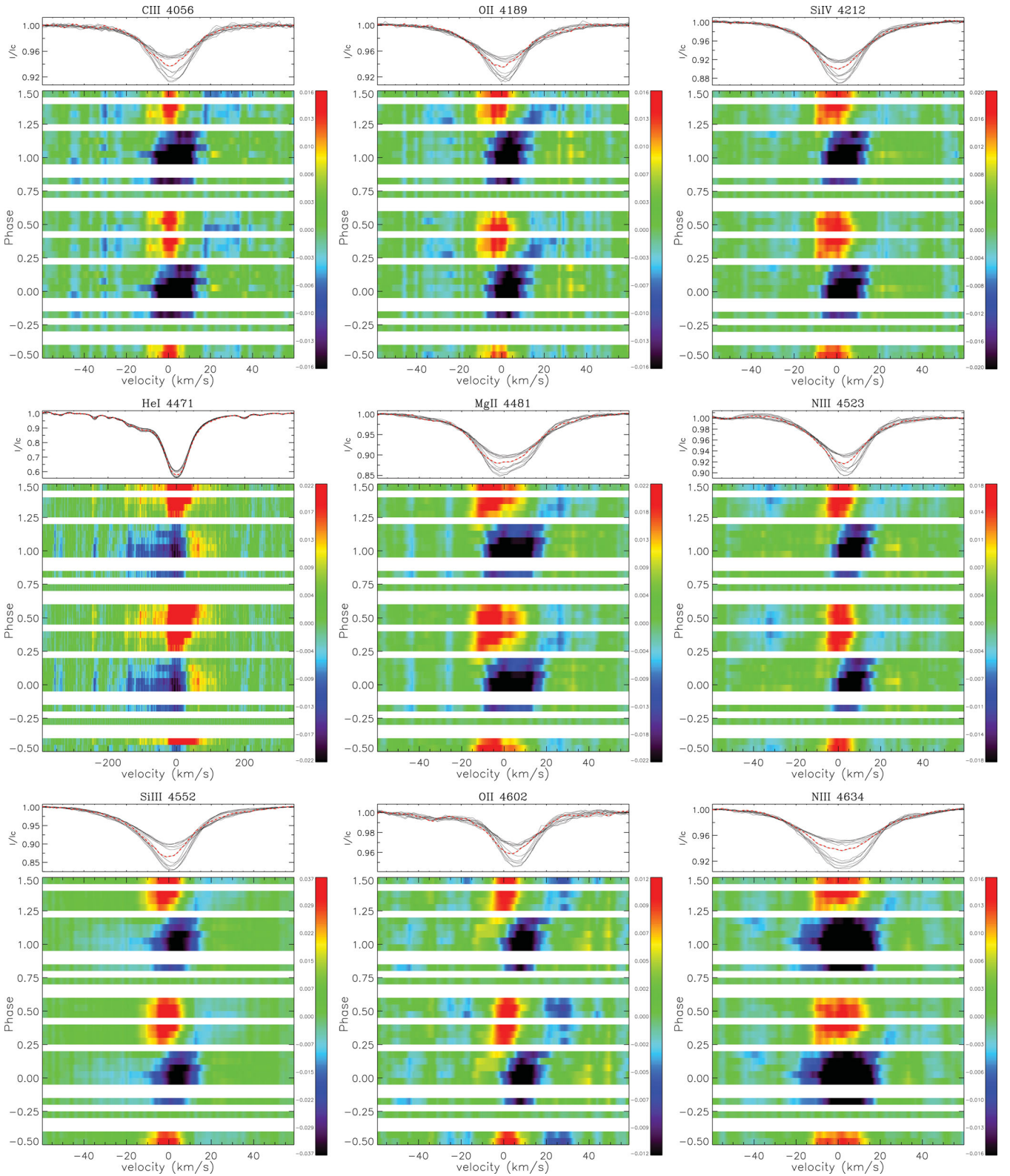
Figure 10. Phased variations in selected spectral lines with sinusoidal EW variations. Plotted is the difference between the observed profiles and the profile obtained on 2010 December 24 (dashed-red, top panel), which occurred at phase ∼0.75, corresponding to when the magnetic equator crosses the line-of-sight.

in a slow rotator such as HD 57682, the transient suspension of wind material in closed magnetic loops, which is constantly fed by the quasi-steady wind outflow, leads to a statistically overdense, low-velocity region in the vicinity of the magnetic equator that

causes persistent, periodic variations of Balmer lines. This method utilizes the two-dimensional (2D) magnetohydrodynamics (MHD) wind simulations of ud-Doula, Owocki & Townsend (2008) and the magnetic parameters determined from the B_ℓ measurements to
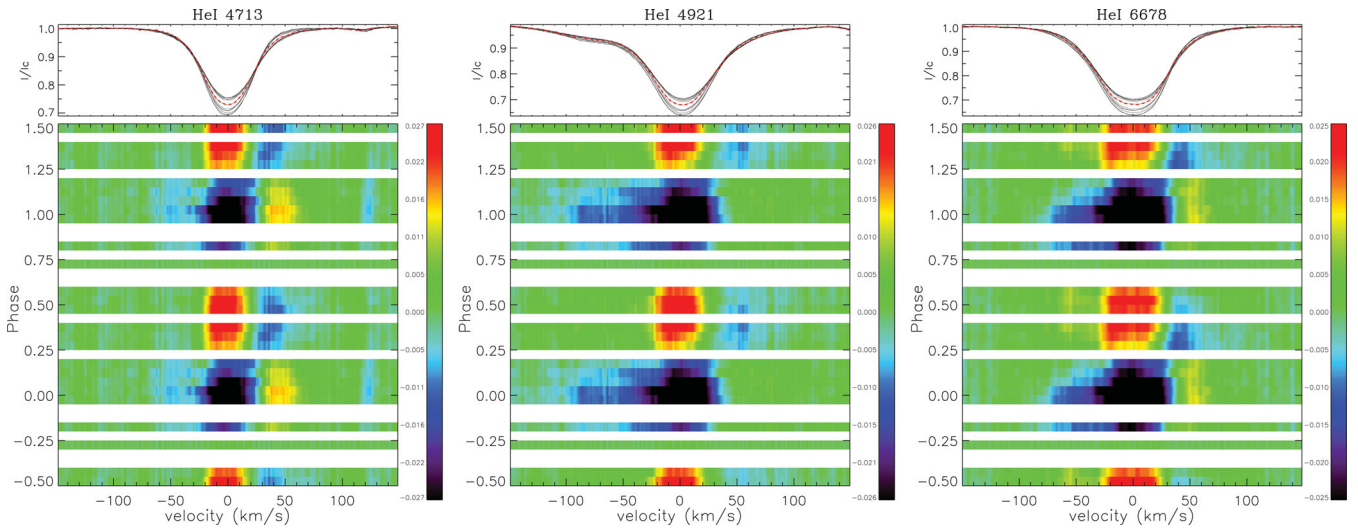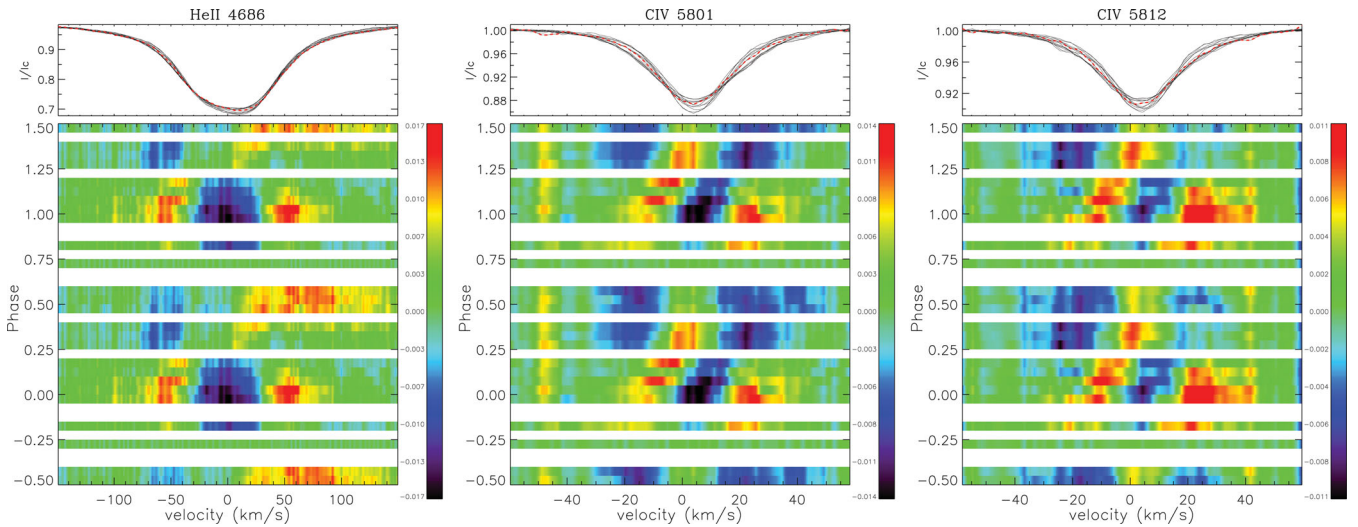
Figure 10 – *continued*

Figure 11. Same as Fig. 10 but for selected spectral lines with clearly non-sinusoidal EW variations or EW variations that appear antiphased with the other lines. Plotted is the difference between the observed profiles and the profile obtained on 2010 December 24 (dashed-red, top panel), which occurred at phase ∼0.75, corresponding to when the magnetic equator crosses the line-of-sight.

determine the properties of the magnetically confined plasma. We note however that the original MHD models were computed for an O-type supergiant. Therefore, in the Hα synthesis here, we have simply re-scaled the Hα scaling invariant $Q = (\dot{M} f_{cl}^2)/(v_\infty R_\star)^{3/2}$ (Puls, Vink & Najarro 2008) from the original simulation to the value obtained for HD 57682 using the parameters of Grunhut et al. (2009). These properties are then used to synthesize the expected Hα line profile as viewed from our line-of-sight as the star rotates. Unlike the 'Toy' model, these simulations are sensitive to the adopted mass-loss rate. We characterize the mass-loss rate as the product of the stellar mass-loss rate and the square root of a wind clumping factor, which we assume to be about 4–10 as suggested by several recent studies (e.g. Bouret et al. 2003; Najarro, Hanson & Puls 2011; Sundqvist et al. 2011a). We attempted to constrain the wind properties by fitting the observed Hα profile during phases that have the lowest contributions from the disc emission. As already noted by Grunhut et al. (2009), we cannot fit the Hα profile using a mass-loss rate as derived from the ultraviolet (UV) lines ($\log \dot{M} \sim -8.85 \, M_\odot \, yr^{-1}$). The additional emission resulting from

the wind is too low at phase 0.25 or 0.75 (minimum emission), which results in a line profile that is mainly in absorption, contrary to what is actually observed (see Fig. 15).

Our results (based on fits to the Hα profile) suggest that the lack of emission is either due to an underestimated stellar mass-loss rate (by a factor of 10–30), or that the wind is very clumpy (note that clumping was not taken into account in the study of Grunhut et al. 2009). This is consistent with many recent studies that find large discrepancies between UV and optical mass-loss rates (see Sundqvist, Owocki & Puls 2011b, and references therein). Furthermore, according to Figs 16 and 17, we find that the model using the UV-derived mass-loss rate produces little to no emission with any significant variability. In fact, the amplitude and the offset of the EW variations shown in Fig. 16 are very sensitive to the adopted mass-loss rate. If we choose a mass-loss rate that best fits the profiles at minimum emission phases, we obtain a mass-loss rate of ∼15 times the suggested UV mass-loss rate (see Fig. 15). However, while the predicted minimum emission of the EW variations is well fit, the maximum emission is underestimated. A mass-loss rate of ∼20
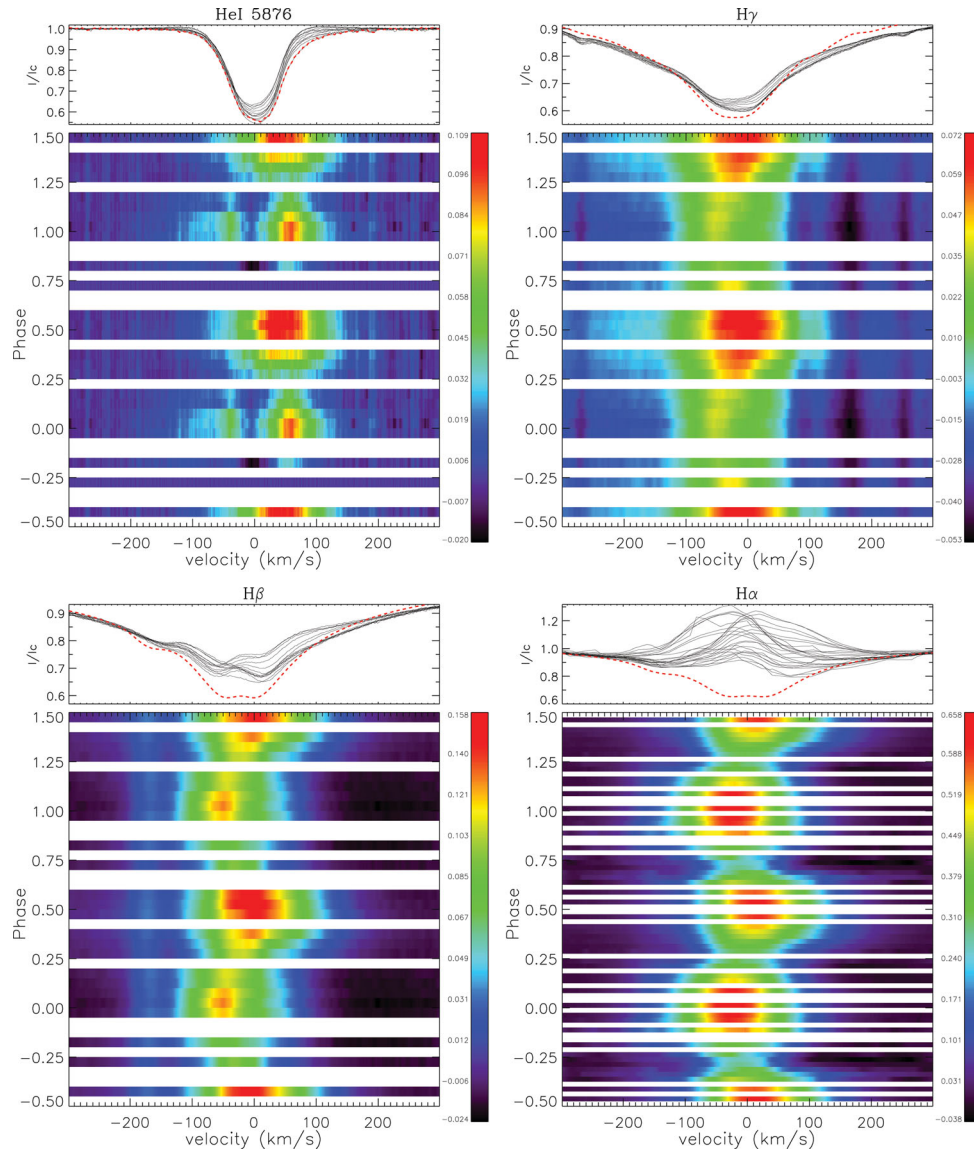
Figure 12. Same as Fig. 10 but for spectral lines that show evidence of two emission features per rotation cycle. The Balmer lines are plotted as the difference between the observed profiles and a NLTE TLUSTY model profile (top panel, dashed-red) to highlight the circumstellar emission. The He I λ5876 lines is plotted as the difference between the observed profiles and the profile obtained on 2010 December 24 (dashed-red, top panel).
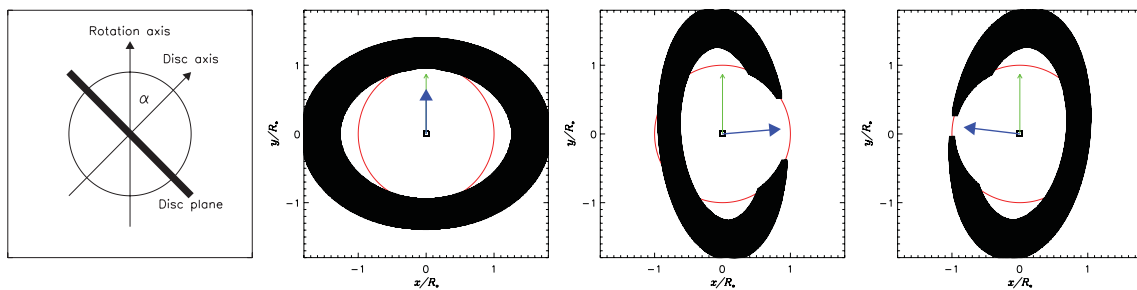
Figure 13. Illustration of our 'Toy' model for the Hα emission disc. The left-hand panel provides an example schematic diagram showing the orientation of the plane of the disc for a given disc inclination α relative to the rotation axis. The other panels represent projections of the disc (solid black) and central star (solid red) on to our line-of-sight during phases 0.0, 0.33 and 0.66. The thin green arrow in these panels represents the projected rotation axis relative to the rotation axis (taken to be 60°), while the thick blue arrow represents the disc axis of 79° relative to the rotation axis.
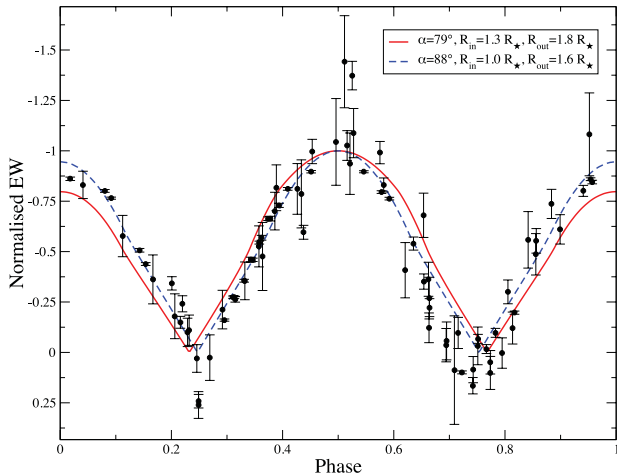
Figure 14. 'Toy' model compared to phased Hα EW measurements (black circles). The solid red curve represents a model with an $\alpha = 79°$ between the rotation axis and the disc axis, as inferred from the fits to the B_ℓ variations, while the dashed blue curve represents the best-fitting model with an $\alpha = 88°$. Both models assume $i = 60°$.
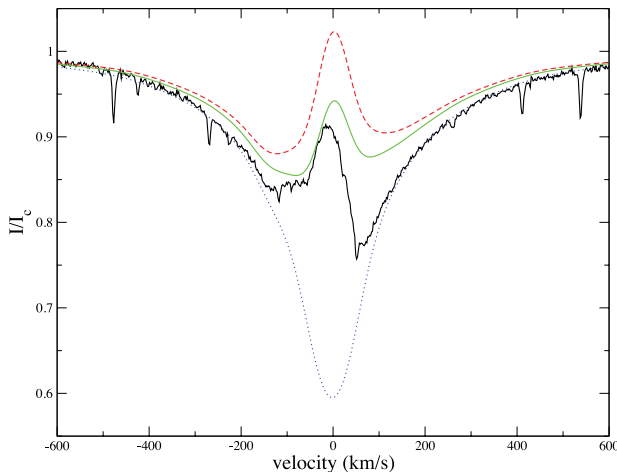
Figure 15. Comparison between observed Hα profile (solid black) from 2010 December 24, corresponding to a phase of 0.72, and synthetic profiles following the procedure of Sundqvist et al. (2012) at this same phase. The model profiles were created with an adopted mass-loss rate as determined by Grunhut et al. (2009) (dotted blue), a mass-loss rate of 17 (solid green) and 21 times this value (dashed red).

times the previous estimate provides a better fit to the EW variations, by underestimating the maximum emission and overestimating the minimum emission. A mass-loss rate of ∼30 times the previously estimated value is needed to provide the correct amplitude of the EW variation, but, as the wind emission is predicted to be significantly higher, there exists a significant offset between the predicted and observed EW values. In any case, our MHD simulations indicate that a higher mass-loss rate than derived by Grunhut et al. (2009) is necessary in order to observe significant variability, with similar characteristics to the observed Hα dynamic spectrum (Fig. 17). The characteristics of the MHD EW curves are similar to the predictions of our 'Toy' model; the phasing of minimum emission is not at phases 0.25 and 0.75 and the relative amplitude of the emission is slightly lower when using $\alpha = 79°$ (note that the pseudo-disc naturally forms along the magnetic equator in these MHD simulations, i.e. $\alpha = \beta$). Just as was found with the 'Toy' model, a higher
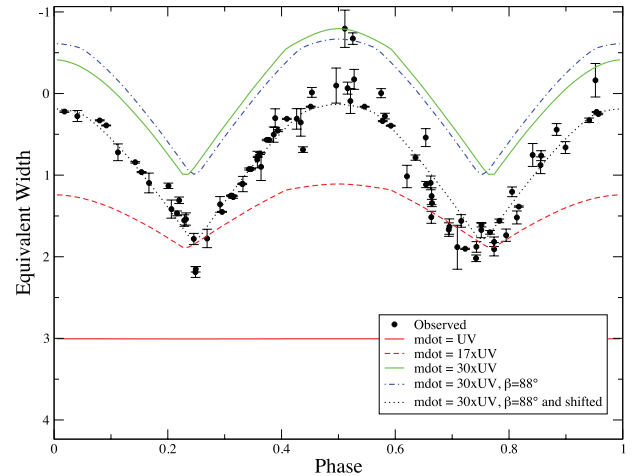
Figure 16. Comparison between the measured EW variations of HD 57682 (black circles) and the theoretical EW variations of our MHD model for different mass-loss rates as labelled (UV corresponds to the UV mass-loss rate derived by Grunhut et al. 2009). While the absolute EW variations of the $\dot{M}/M_\odot = 30\times$ UV (dash–dotted blue) model do not fit the observed EW curve, the amplitude of the predicted variations from this model does provide a good fit, as illustrated for the same model but vertically shifted to better match the variations implied by the observations (black dotted line).

$\beta = 88°$ provides a better agreement with observations. Of particular interest, is the fact that the synthesized emission variation in Fig. 17 is predicted to be symmetric about the systemic velocity of HD 57682 with the adopted high β. However, a lower β does provide increased occultation of the disc and therefore necessarily results in a more asymmetric line profile variation at some phases, similar to the observations.

7.2 Greater circumstellar region

We continued our investigation of the circumstellar environment to larger distances as probed at IR wavelengths. Our original intention was to investigate the IR properties of HD 57682's SED to address the uncertain classification of HD 57682 as a classical Oe star and to potentially probe the extent of the magnetosphere.

In Fig. 18, we show the SED of HD 57682 from the UV to IR wavelengths. The data were collected from the *IUE* data base and the available photometric archives discussed in Section 2. Also included in this figure are theoretical SEDs based on the original stellar parameters of Grunhut et al. (2009) and updated values presented here. A comparison between our CMFGEN (Hillier & Miller 1998) model with the newly inferred parameters and the *IUE* data is also presented in the lower panel of this figure, illustrating the agreement between the observations and the model. We note that we have still adopted the lower UV mass-loss rate of Grunhut et al. (2009) in this CMFGEN model. Our new model has revised the distance and reddening parameters of Grunhut et al. (2009, $d \sim 1.3$ kpc, $E(B - V) = 0.07$), which were only derived from the *IUE* data and do not provide a good fit to the photometric measurements blue-ward of 50 000 Å (5 μm). Our revised parameters are $d \sim 1.0$ kpc and $E(B - V) = 0.12$. The SED also shows a large disagreement between the *IRAS* and *WISE* data points, but this reflects the variation in the aperture sizes of the different instruments; the *IRAS* aperture is about five times larger and therefore includes more contribution of circumstellar emission (as further discussed below), while *WISE* measurements represent more of the true 'stellar' flux, and
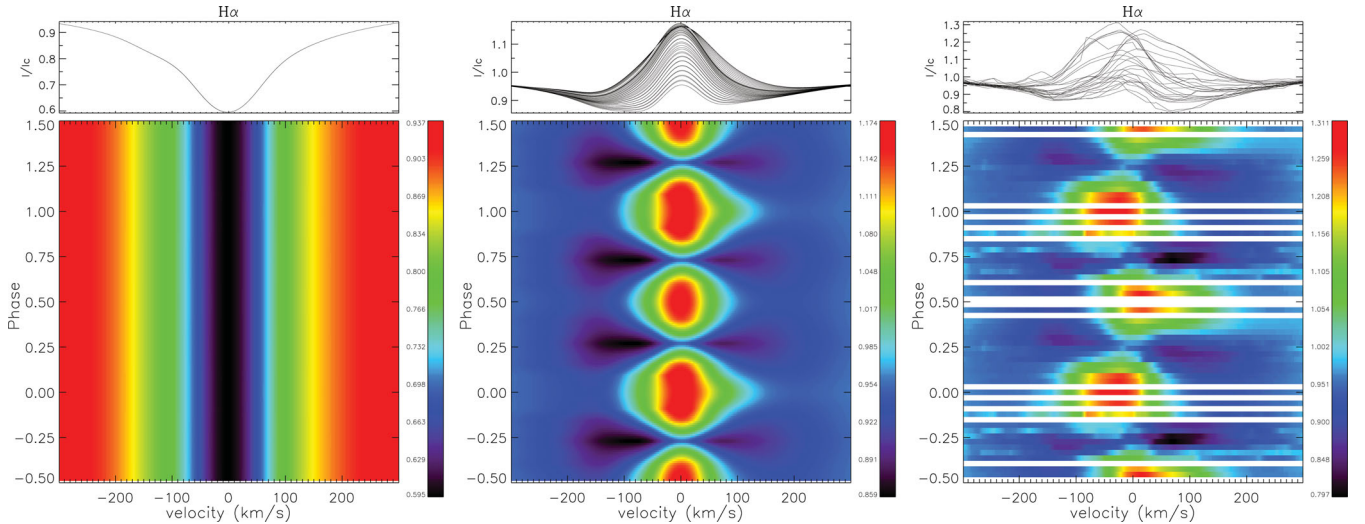
Figure 17. Rotationally phased variations in observed (right-hand panel) and modelled Hα profiles. The model in the left-hand panel shows the predicted variations assuming the mass-loss rate of Grunhut et al. (2009), while the central panel uses an adopted mass-loss rate of 21 times this value. Note the lack of predicted variations of the model adopting the mass-loss rate of Grunhut et al. (2009) and the predicted emission symmetry.
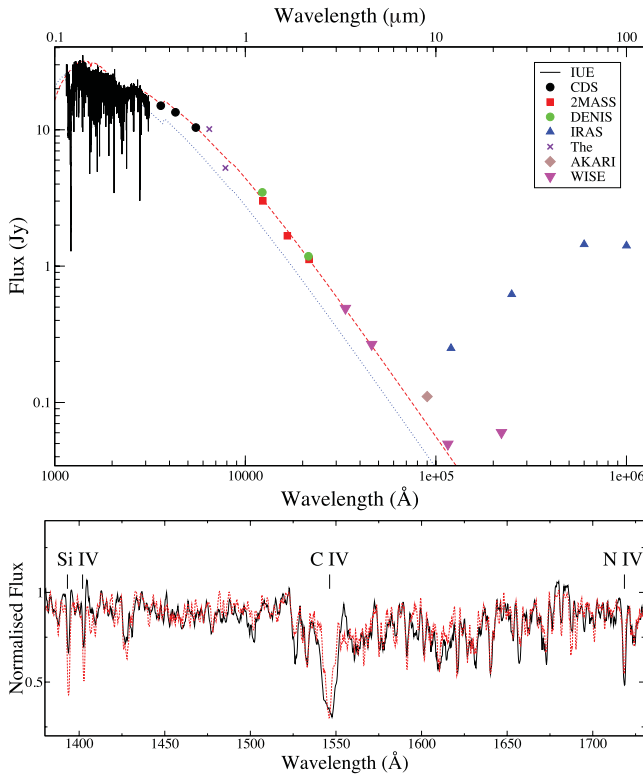

Figure 18. Upper: observed *IUE* observations and IR flux measurements from the indicated sources. Also included are stellar models corresponding to the parameters derived by Grunhut et al. (2009) ($d = 1.3$ kpc and $E(B - V) = 0.07$; dashed grey) and the revised model presented here ($d = 1.0$ kpc and $E(B - V) = 0.12$; dashed red). The larger flux of the *IRAS* data points compared to the *WISE* measurements reflects the significantly larger aperture and therefore increased contribution from the surrounding emission. Lower: comparison between the observed *IUE* spectrum (solid black) and the CMFGEN model with the parameters inferred in this work (dashed red) in the wavelength range of 1380–1730 Å. The CMFGEN model still adopts the lower mass-loss rate of Grunhut et al. (2009) and not the higher value needed to fit Hα (Fig. 15; see Section 7 for further discussion). Both the model and observed spectrum were smoothed for display purposes.

appear consistent with the other IR measurements. The observed SED does show a large disagreement with the theoretical SED for measurements red-ward of 1×10^5 Å (10 μm). The observed IR emission appears to be increasing with increasing wavelength and not decreasing as predicted by contributions from pure stellar flux, and therefore represents an additional source of emission.

In order to better understand the characteristics of the IR excess we utilized the procedure of Ignace & Churchwell (2004) to model the free–free emission that would be emitted from a spherical cloud; IR excess is common amongst Be/Oe stars and is caused by free–free emission from the circumstellar disc. Using this procedure we find that we can qualitatively match the characteristics of the IR excess by varying the properties of the cloud. A brief investigation of this model shows that the location of the IR bump is mainly controlled by the temperature of the cloud (we find $T \sim 20\,000$ K to be sufficient), but the size of the bump is controlled by the relative sizes of the cloud and star. For simplicity we assume that the cloud is of constant density, which then requires a cloud of approximately $100 R_\star$ to reproduce the observations. If we instead adopt a cloud with many large clumps of different densities and at different radii (as is done in Ignace & Churchwell 2004) we can achieve similar results without the need for a $100 R_\star$ cloud. However, if we assume that the cloud is not highly clumped and results from stellar mass lost by HD 57682, this would imply an unreasonable mass for the cloud, suggesting that HD 57682 is in fact not a classical Oe star.

In light of this conclusion we further investigated the *IRAS* photometry. In the end we suspect that the additional emission is a result of HD 57682's illumination of the IC 2177 nebula (Halbedel 1993). A look at the HIRES/*IRAS* maps, as shown in Fig. 19, shows significant IR emission centred on HD 57682 at 25 and 60 μm, with the size of the emission cloud larger at 60 μm. Emission is also evident at 12 μm, but does not reach the same spatial extent as found at 25 or 60 μm. At 100 μm the cloud overwhelms the field of view (30×30 arcmin^2), but appears to be a blend of several clouds. It is also evident from these images that the majority of the point sources in the field of view are illuminating the nebula at these wavelengths, further corroborating our suggestion that the IR emission does not result from a circumstellar disc or even the extended magnetosphere of HD 57682.
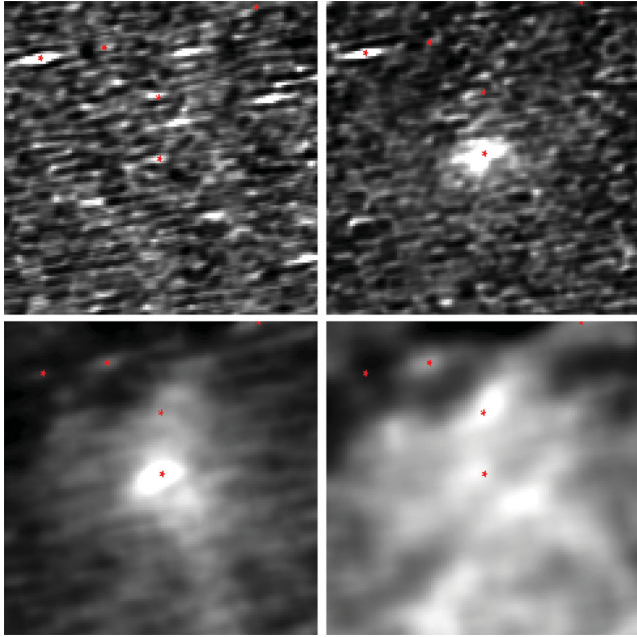
Figure 19. IR emission as detected by *IRAS*/HIRES at different wavelengths (top left – 12 μm; top right – 25 μm; bottom left – 60 μm; bottom right – 100 μm). Each image represents a 30×30 arcmin^2 scale. Point sources are indicated by the red circles and the field of view is centred on HD 57682. Note that the elliptical shape of the point sources is a result of the scanning direction of the *IRAS* detector.

8 DISCUSSION AND CONCLUSIONS

In this paper we report on our ongoing work towards understanding the magnetic properties and variability of the magnetic O9 subgiant star HD 57682. Our current analysis is based on an extensive data set spanning almost 15 yr, including archival spectra from ESO's CES, UVES and FEROS spectrographs, and from the echelle spectrograph at LCO. In addition numerous low-resolution spectra were acquired and accessed from the BeSS data base. Furthermore, we also present 13 newly obtained, high-resolution spectropolarimetric observations acquired with ESPaDOnS at the CFHT within the context of the MiMeS project.

A period analysis performed on the spectroscopic Hα EW variations and the polarimetric B_ℓ measurements resulted in a single, consistent period between the polarimetric and Hα variations of 63.5708 ± 0.0057 d, which we infer to be the rotational period of this star. This long rotational period suggests that the $v \sin i$ inferred by Grunhut et al. (2009) is too high by a factor of $\sim$2, which led us to attempt to remeasure this value. We found that the C IV λ5801 photospheric line was the least susceptible to additional macroturbulence in the line profile and therefore we were able to estimate a new $v \sin i = 4.6 \pm 0.6$ km s^{-1}, which is now consistent with the $\sim$63 d period. This period also implies that the inclination of the rotation axis $i > 30°$ with a best-fitting value $i \sim 56°^{+34°}_{-26°}$.

From fits to the rotationally phased B_ℓ measurements we were able to constrain the magnetic dipole parameters of HD 57682, assuming that the magnetic field is well characterized by the ORM. Taking $i = 60°$, the data imply that $B_d = 880 \pm 50$ G and $\beta = 79° \pm 4°$. However, direct modelling of the individual mean LSD profiles suggests a somewhat weaker dipole field strength of $\sim$700–900 G and a smaller obliquity angle of $\sim$60°–68°. However, the results are strongly dependent on the adopted depth and width of the modelled LSD Stokes I and V profiles, as discussed in Section 5. Therefore, it

is likely that improved modelling of the observed line profiles that correctly takes into account the profile variations could reduce the disagreement and we therefore suggest that the real magnetic dipole parameters are closer to the parameters implied by the B_ℓ variation.

The profile variations of nearly all observable lines in the high-resolution ESPaDOnS spectra were also investigated (Figs 8 and 9). Our analysis suggests that we can essentially separate all lines into one of two categories as determined by the rotationally phased EW variations of the spectral line. There are those lines that show clear evidence of double-peaked variations similar to Hα, while the rest show single-peaked, sinusoidal variations. The LPV of these lines, as described in Section 6, shows rotationally phased velocity variations of the pseudo-absorption or pseudo-emission components, and the pattern of this variability is generally consistent amongst all the lines.

In Section 7, we clearly showed that the double-peaked variations of the Hα EW are well explained by the presence of the variable projection of a flattened distribution of magnetospheric plasma trapped in closed loops near the magnetic equatorial plane. This flattened distribution is also predicted by MHD simulations using the stellar and magnetic properties as determined here and by Grunhut et al. (2009), although we find that a mass-loss rate that is 20–30 times greater than the value inferred by Grunhut et al. (2009) from the UV lines is necessary to produce the level of emission that is observed. However, at present we are not able to model UV resonance lines using our MHD wind simulation and therefore must resort to modelling these lines using a spherically symmetric wind model. The predicted UV spectrum, as modelled using CMFGEN, indicates the presence of several intense spectral emission lines that are observed mainly in absorption in the *IUE* spectrum (e.g. Si IV λ1400 and N IV λ1718) or that the observed lines are too weak (e.g. N V λ1240 and C IV λ1550). However, the *IUE* spectrum is well reproduced when adopting the lower mass-loss rate, as already demonstrated by Grunhut et al. (2009) and illustrated in the lower panel of Fig. 18. Note that CMFGEN assumes a spherically symmetric wind, whereas the MHD wind simulations predict a highly non-spherical wind with important consequences for spectral line diagnostics (ud-Doula & Owocki 2002; Sundqvist et al. 2012). Furthermore, the UV lines are very sensitive to the ionization structure of the wind, which may also be largely affected by a non-spherically symmetric wind. This is not the case for Hα as it is a recombination-based optical emission line, which is insensitive to the exact modelling of the ionization structure (e.g. Sundqvist et al. 2012). Therefore it is not surprising that there is a disagreement between the mass-loss rates inferred by our optical and UV analyses. Future MHD UV line modelling will be necessary to resolve this discrepancy.

The MHD model provides not only an independent analysis of the stellar mass-loss rate, but also of the magnetic geometry, which is constrained by the characteristics of the Hα EW variations. Using the higher mass-loss rate shows that the Hα emission variation can be reasonably modelled, however, there are several inconsistencies between the models and observed data that reflect our uncertainty in the mass-loss rate and potentially the magnetic geometry. Our results show that the inclination of the disc relative to the rotation axis must be greater than the inferred magnetic obliquity (as measured from our polarimetric data), since a higher disc inclination provides a much better fit to the observed EW variations. This may also be attributed to warping of the disc, or may even reflect the fact that the disc does not necessarily lie in the magnetic equatorial plane as predicted by MHD simulations.

As with the LPV for the sinusoidally varying lines, there also appears to be rotationally phased velocity variations in the position

of the central emission component in the Hα line profile that is not predicted by the MHD simulations. We discuss a few potential explanations. If the disc structure is not vertically symmetric along the rotation axis (i.e. not symmetric about the equatorial rotation plane) the resulting line profiles would be asymmetric and would result in velocity shifting of the disc emission. Likewise, enhanced emission from a non-uniform velocity flow where the velocity flow occurs at high magnetic latitudes could also explain our observations. For example, during phases where the disc is viewed nearly face on, the emission could appear systematically offset from the systemic velocity if there is an additional outflow or inflow, for instance, due to the stellar wind or circumstellar plasma falling back on to the star. This would result in no velocity offset during phases where the disc is viewed nearly edge on as the additional outflow or inflow would appear perpendicular to our line-of-sight. However, it is difficult to understand a scenario where there would be a preference for outflow or inflow of plasma at one magnetic hemisphere compared to the other. This is required to explain the velocity shifting of the emission that occurs as our line-of-sight rotates from one magnetic hemisphere to the other. Another possible solution is to introduce an offset of the dipole relative to the centre of the star. Our preliminary tests suggest that a small offset of $\sim 0.2\,R_\star$ along the rotation axis could explain the velocity shifting of the emission that is observed in Hα, although MHD models implementing this offset are necessary to confirm this phenomenon, which will be the subject of future studies.

In addition to the LPV, we also measure RV variability in nearly all spectral lines and find that all lines with sinusoidally varying EW measurements show approximately sinusoidally varying RV measurements. Turner et al. (2008) investigated the binarity of this star and found no evidence of a companion in either their *I*-band adaptive optics or RV measurements. If we assume that the RV variations are due to a binary companion, a least-squares analysis of the RV measurements obtained from the mean LSD *I* profile would suggest a mass function $f(M/M_\odot) = 2.2 \pm 0.9 \times 10^{-6}$ for the companion star. For reasonable orbital inclinations, this would require the companion to be a very low-mass (and presumably a low-luminosity) star, and therefore should not have a significant effect on the observed line profile, which we clearly do observe. Taking this into account, it is therefore unlikely that the RV variations are due to a binary companion since we do not observe clear shifts of the entire spectroscopic lines. We propose that the RV variations are likely a result of the variable asymmetry of the line profiles and simply reflect the varying location of the centre-of-gravity in the profiles. This is clearly evident in the lines that show a double-wave EW curve since the RV measurements also show a more complex double-wave pattern. Furthermore, there also appears to be more of a direct relationship between the RV and EW measurements in these lines, while the majority of the sinusoidally varying lines show a ~ 0.25 phase offset between the RV and EW variations.

The root cause of the LPV in the sinusoidally varying lines is still an outstanding issue. It is highly unlikely that these variations are caused by surface features (e.g. chemical 'spots') as the observed variability between multiple ions of a given species does not behave as predicted by LTE or NLTE spectrum synthesis. For example, our observations demonstrate that the weak N IV λ4058 line exhibits the same relative EW variation as the strong N III λ4523 line, but spectral modelling of these lines shows that the weaker line should show 30 per cent stronger variation if due to abundance changes. Furthermore, the strong Si IV λ4115 line and the weak Si IV λ4403 line show nearly the same level of EW modulation, but the weak Si IV line should show a 60 per cent larger amplitude in the EW variation if

resulting from abundance changes. The weak Si IV λ4667 line is also predicted to show the same relative EW variation as the λ4403 line, but our observations show a significantly greater level of variability (about 50 per cent larger) in the λ4667 line. Moreover, abundance spots require that all spectral lines of a given species vary in phase. This is clearly not the case for the C IV lines (5801, 5811 Å) that vary in antiphase with the C III lines (as shown in Fig. 8), or the N IV λ4058 and N III λ4523 lines, which appear shifted relative to one another by a quarter of a cycle. The interpretation of the variability in terms of surface spots would also imply that all elements (except perhaps C) are concentrated at the same general region on the stellar surface, which would be a remarkable new phenomenon. Another possibility is that the variations may result from pulsations; however, pulsations should occur on much shorter time-scales (e.g. Aerts, Christensen-Dalsgaard & Kurtz 2010). The rotationally phased, double-peaked EW variations are well explained by the variable projection of a flattened distribution of magnetospheric plasma, and at first glance it is difficult to apply this same disc model to explain the variations in the other lines. Occultation or variable emission from a symmetric disc would result in double-peaked variations in all lines and not the single-peaked emission that we observe. However, the LPV of the higher Balmer lines (Fig. 12) likely provide the link between the double-peaked variability and single-peaked variability; a decrease in the strength of the emission feature at phase 0.25 and 0.75 compared to the emission feature at phase 0 is clearly observed in higher Balmer lines. Furthermore, this is also illustrated in the EW variations of the Balmer lines (Figs 8 and 9), which show a clear transition from the double-peaked EW curve at Hα to a single-peaked curve at Hγ. Therefore, we tentatively conclude that all line profile variability observed in HD 57682 is a result of variations of the flattened distribution of magnetospheric plasma. The details of the variable emission for different lines likely reflect the fact that each line probes a different region of what is likely an asymmetric spatial or velocity distribution of the magnetospheric plasma and that the disc is not completely optically thick for all lines-of-sight, for all wavelengths. We suspect that full three-dimensional (3D) MHD models and an extension of the line profile synthesis techniques of Sundqvist et al. (2012) to lines other than Hα are necessary to properly model these properties.

In summary, the narrow-lined photospheric spectrum and weak wind of HD 57682 have allowed us to study its magnetic and magnetospheric properties at a level of detail not currently achievable for any other magnetic O-type star. The results of our analysis indicate a highly complex behaviour that can be used as a test bed for future more sophisticated 3D MHD simulations to better understand non-rotationally supported magnetospheres (also referred to as dynamical magnetospheres; Petit et al. 2011; Sundqvist et al. 2012) of hot stars.

REFERENCES

Aerts C., Christensen-Dalsgaard J., Kurtz D. W., 2010, Asteroseismology. Springer-Verlag, Heidelberg

Bagnulo S., Landstreet J. D., Fossati L., Kochukhov O., 2012, A&A, 538, 129

Bouret J.-C., Lanz T., Hiller D. J., Heap S. R., Hubeny I., Lennon D. J., Smith L. J., Evans C. J., 2003, ApJ, 595, 1182

Bouret J.-C., Donati J.-F., Martins F., Escolano C., Marcolino W., Lanz T., Howarth I. D., 2008, MNRAS, 389, 75

Claret A., 2000, A&A, 363, 1081

Donati J.-F., Semel M., Carter B. D., Rees D. E., Collier Cameron A., 1997, MNRAS, 291, 658

Donati J.-F., Wade G. A., Babel J., Henrichs H. F., de Jong J. A., Harries T. J., 2001, MNRAS, 326, 1265

Donati J.-F., Babel J., Harries T. J., Howarth I. D., Petit P., Semel M., 2002, MNRAS, 333, 55

Donati J.-F., Howarth I. D., Bouret J.-C., Petit P., Catala C., Landstreet J., 2006, MNRAS, 365, L6

Fullerton A. W., Petit V., Bagnulo S., Wade G. A., 2011, in Neiner C., Wade G., Meynet G., Peters G., eds, Proc. IAU Symp. 272, Active OB Stars. Cambridge Univ. Press, New York, p. 182

Gray D. F., 1981, ApJ, 251, 155

Grunhut J. H. et al., 2009, MNRAS, 400, L94

Halbedel E. M., 1993, Inf. Bull. Var. Stars, 3850, 1

Hillier D. J., Miller D. L., 1998, ApJ, 496, 407

Howarth I. D. et al., 2007, MNRAS, 381, 433

Hubrig S., Schöller M., Schnerr R. S., González J. F., Ignace R., Henrichs H. F., 2008, A&A, 490, 793

Hubrig S., Oskinova L. M., Schöller M., 2011a, Astron. Nachr., 332, 147

Hubrig S. et al., 2011b, A&A, 528, 151

Ignace R., Churchwell E., 2004, ApJ, 610, 351

Jankov S., 1995, Publ. Obser. Astron. Belgrade, 50, 75

Kaper L., Fullerton A. W., Baade D., 1998, in Kaper L., Fullerton A. W., eds, Proc. ESO Workshop on Cyclical Variability in Stellar Winds. Springer-Verlag, New York, p. 103

Kochukhov O., 2007, in Romanyuk I. I., Kudryavstev D. O., eds, Proc. Int. Conf. Physics of Magnetic Stars. p. 109

Lanz T., Hubeny I., 2003, ApJS, 146, 417

Martins F., Donati J.-F., Marcolino W. L. F., Bouret J.-C., Wade G. A., Escolano C., Howarth I. D., the MiMeS Collaboration, 2010, MNRAS, 407, 1423

Najarro F., Hanson M. M., Puls U., 2011, A&A, 535, 32

Nazé Y., Bagnulo S., Petit V., Rivinius Th., Wade G., Rauw G., Gangé M., 2012, MNRAS, 423, 3413

Perryman M. A. C. et al., 1997, The Hipparcos and Tycho Catalogues, ESA SP-1200. ESA, Noordwijk

Petit V., Wade G. A., 2012, MNRAS, 420, 773

Petit V., Owocki S. P., Oksala M. E., the MiMeS Collaboration, 2011, in ASP Conf. Ser., Four Decades of Research on Massive Stars. Astron. Soc. Pac., San Francisco, in press

Piskunov N. E., Kupka F., Ryabchikova T. A., Weiss W. W., Jeffery C. S., 1995, A&AS, 112, 525

Press W. H., Teukolsky S. A., Vetterling W. T., Flannery B. P., 1992, Numerical Recipes in FORTRAN, 2nd edn. Cambridge Univ. Press, Cambridge

Puls J., Vink J. S., Najarro F., 2008, A&AR, 16, 209

Rees D. E., Semel M. D., 1979, A&A, 74, 1

Schwarzenberg-Czerny A., 1996, ApJ, 460, L107

Simón-Díaz S., Herrero A., 2007, A&A, 468, 1063

Stahl O. et al., 1996, A&A, 312, 539

Sundqvist J. O., Puls J., Feldmeier A., Owocki S. P., 2011a, A&A, 528, 64

Sundqvist J. O., Owocki S. P., Puls J., 2011b, in ASP Conf. Ser., Four Decades of Research on Massive Stars. Astron. Soc. Pac., San Francisco, in press

Sundqvist J. O., ud-Doula A., Owocki S. P., Townsend R. H. D., Howarth I. D., Wade G. A., the MiMeS Collaboration, 2012, MNRAS, 423, L21

The P. S., Wesselius P. R., Janssen I. M. H. H., 1986, A&AS, 66, 63

Turner N. H., Brummelaar A. T., Roberts L. C., Mason B. D., Hartkopf W. I., Gies D. R., 2008, AJ, 136, 554

ud-Doula A., Owock S. P., 2002, ApJ, 576, 413

ud-Doula A., Owocki S. P., Townsend R. H. D., 2008, MNRAS, 385, 97

Wade G. A., Fullerton A. W., Donati J.-F., Landstreet J. D., Petit P., Strasser S., 2006, A&A, 451, 195

Wade G. A. et al., 2011, MNRAS, 416, 3160

Wade G. A. et al., 2012a, MNRAS, 419, 2459

Wade G. A. et al., 2012b, MNRAS, 425, 1278

Wade G. A., Grunhut J. H., the MiMeS Collaboration, 2012c, in Proc. Circumstellar Dynamics at High Resolution, preprint (arXiv:1206.5163)

APPENDIX A: Hα EQUIVALENT WIDTH MEASUREMENTS

Table A1. Spectroscopic Hα EW measurements. Included is the instrument or observatory name, the heliocentric Julian date and the measured Hα EW and its corresponding 1σ uncertainty.

Instrument	HJD	Hα EW (Å)	σ_{EW} (Å)
CES	245 0125.6216	1.270	0.014
CES	245 0126.6291	1.108	0.007
CES	245 0127.6296	0.926	0.008
CES	245 0128.6284	0.735	0.012
CES	245 0129.6287	0.569	0.011
CES	245 0130.6194	0.454	0.010
CES	245 0131.6155	0.311	0.007
UVES	245 2621.8553	0.278	0.035
FEROS	245 3042.6286	1.130	0.033
FEROS	245 3043.6016	1.468	0.029
FEROS	245 3045.6764	2.187	0.066
FEROS	245 3045.6873	2.154	0.034
FEROS	245 3361.6916	1.308	0.040
LCO	245 5111.8964	1.612	0.015
LCO	245 5112.8549	1.701	0.019
LCO	245 5113.8919	1.560	0.019
BeSS	245 4786.6621	0.785	0.032
BeSS	245 5233.4387	1.517	0.074
BeSS	245 5233.4676	1.259	0.103
BeSS	245 5233.4960	1.341	0.045
BeSS	245 5235.3993	1.667	0.083
BeSS	245 5235.4449	1.630	0.094
BeSS	245 5238.4500	2.019	0.041
BeSS	245 5238.4842	1.880	0.065
BeSS	245 5240.4484	1.816	0.058
BeSS	245 5240.4492	1.908	0.082
BeSS	245 5242.4600	1.205	0.059
BeSS	245 5247.4463	0.441	0.072

Table A1 – *continued*

Instrument	HJD	Hα EW (Å)	σ_{EW} (Å)
BeSS	245 5248.4281	0.662	0.073
BeSS	245 5257.4440	0.276	0.068
BeSS	245 5269.3994	1.556	0.070
BeSS	245 5270.4613	1.783	0.069
BeSS	245 5273.3852	1.358	0.096
BeSS	245 5279.3785	0.503	0.093
BeSS	245 5282.4116	0.354	0.169
BeSS	245 5286.3735	−0.097	0.215
BeSS	245 5287.3461	−0.794	0.228
BeSS	245 5288.3862	−0.174	0.122
BeSS	245 5291.3937	−0.004	0.055
BeSS	245 5296.3850	0.540	0.110
BeSS	245 5296.4176	1.115	0.038
BeSS	245 5300.3406	1.561	0.077
BeSS	245 5305.3715	1.736	0.075
BeSS	245 5308.3416	0.753	0.140
BeSS	245 5315.3491	−0.163	0.206
BeSS	245 5519.7252	1.096	0.121
BeSS	245 5542.5156	−0.673	0.071
BeSS	245 5548.5674	1.016	0.137
BeSS	245 5563.5060	0.878	0.103
BeSS	245 5563.5549	0.762	0.061
BeSS	245 5587.4412	1.537	0.075
BeSS	245 5595.4170	0.810	0.102
BeSS	245 5597.4102	0.301	0.114
BeSS	245 5600.5138	0.687	0.034
BeSS	245 5601.5064	−0.014	0.060
BeSS	245 5605.4999	−0.066	0.074
BeSS	245 5620.4429	1.673	0.094
BeSS	245 5624.4170	1.519	0.079
BeSS	245 5643.4021	0.720	0.102

Table A1 – *continued*

Instrument	HJD	Hα EW (Å)	σ_{EW} (Å)
BeSS	245 5649.3697	1.416	0.111
BeSS	245 5653.3678	1.775	0.113
BeSS	245 5657.3714	1.109	0.094
BeSS	245 5659.3947	0.897	0.169
BeSS	245 5663.3730	0.311	0.126
BeSS	245 5669.3974	0.092	0.152
BeSS	245 5678.3725	1.095	0.084
BeSS	245 5681.3408	1.884	0.269
ESPaDOnS	245 4806.0798	0.328	0.027
ESPaDOnS	245 4807.1081	0.251	0.009
ESPaDOnS	245 4955.7675	1.450	0.005
ESPaDOnS	245 4956.7498	1.251	0.006
ESPaDOnS	245 4958.7805	0.924	0.012
ESPaDOnS	245 4959.7489	0.777	0.007
ESPaDOnS	245 4960.7480	0.569	0.009
ESPaDOnS	245 5197.0957	0.391	0.005
ESPaDOnS	245 5201.0427	0.963	0.007
ESPaDOnS	245 5219.9544	0.162	0.006
ESPaDOnS	245 5225.9835	0.161	0.005
ESPaDOnS	245 5228.0015	0.338	0.007
ESPaDOnS	245 5228.9031	0.395	0.007
ESPaDOnS	245 5251.9131	0.226	0.007
ESPaDOnS	245 5255.9893	0.223	0.008
ESPaDOnS	245 5259.9422	0.327	0.007
ESPaDOnS	245 5263.9098	0.843	0.009
ESPaDOnS	245 5529.0354	1.251	0.007
ESPaDOnS	245 5555.0640	1.904	0.007
ESPaDOnS	245 5561.0733	1.387	0.008

This paper has been typeset from a TeX/LaTeX file prepared by the author.